

Validation of
the Lowered Acoustic Doppler Current
Profiler
Finescale Response Function

Xin Li

Universität Bremen, 2005

Validation of
the Lowered Acoustic Doppler Current
Profiler
Finescale Response Function

Master Thesis

Institute of Environmental Physics

University of Bremen

Xin Li

- 1.Referee: Prof. Dr. M. Rhein
- 2.Referee: Prof. Dr. J. Notholt

Submit Date: 2005-08-09

Contents

1	Introduction	7
2	Mixing and Internal Waves	9
2.1	Mixing	9
2.1.1	The Importance of Vertical Mixing	10
2.1.2	Estimated and Measured Vertical Mixing	10
2.2	Internal waves	13
2.2.1	The Internal Wave Field	13
2.2.2	Wave Spectrum	14
2.2.3	The Garrett and Munk Model	15
2.2.4	Shear and Strain Spectra	16
2.2.5	Inferring Eddy Diffusivity	18
3	Measurements	20
3.1	Expendable Current Profiler	20
3.1.1	Theory of Operation	20
3.1.2	Instrumentation	22
3.1.3	Accuracy and Performance of XCP	22
3.2	Lowered Acoustic Doppler Current Profilers	23
3.2.1	Doppler Effect	23
3.2.2	Three-dimensional Current Velocity Vectors	25
3.2.3	Velocity Profile	26
3.2.4	Data Processing	29
3.3	CTD	31
4	The Model of Polzin et al.	32
4.1	Transfer Functions for Data Processing	32
4.2	Transfer Function for Tilting	34
4.3	Transfer Function for Beam Separation Effect	35
4.4	Model Summary	35

5	Results	37
5.1	Data	38
5.2	Comparison of Velocity Profiles	39
5.3	Spikes in XCP velocity spectra	42
5.4	Comparison of Shear Spectra	45
5.4.1	Prior to Estimation of Shear Spectra	45
5.4.2	Computation of Buoyancy Frequency	46
5.4.3	Coherence Spectrum of XCP and LADCP profiles	46
5.4.4	Shear Spectra of XCP and LADCP Profiles	47
5.4.5	Comparison with Strain Spectra	55
5.4.6	Comparison with Eddy Diffusivities	56
6	Summary and Conclusions	59
	Acknowledgments	61
	Bibliography	62

List of Figures

2.1	Various processes which are associated with mixing in the ocean. Figure taken from the web site of the University of Washington.	9
2.2	Schematic showing the meridional overturning circulation in the Southern Ocean (Gargett 1998).	11
2.3	A section of turbulent diffusivity across the Brazil Basin. The diffusivity estimates were made using observation of velocity measurements which were averaged into 200 m vertical bins. (Polzin and Firing, 1997).	12
2.4	A composite spectrum of vertical shear of horizontal velocity (Gargett et al., 1981).	17
3.1	Left: XCP launch sequence from underway vessel. Right: XCP schematic (Sanford et al., 1993).	21
3.2	A photo of CTD-ADCP instrument package. The two yellow ADCPs are attached to rosette frames in opposite direction (one upward and the other downward). Photo is given by O. Bislich.	24
3.3	Schematic drawing depicting the measurement of relative velocity on the basis of acoustic Doppler effect. The ADCP measures only the velocity component parallel to the acoustic beams (RDI, 1996).	24
3.4	Schematic of the LADCP measurement geometry (Polzin et al., 2002).	25
3.5	ADCP sensor head. The red circles denote the 4 transducer faces (The Figure is taken from the website of the RDI).	26
3.6	Measurement scheme with lowered CTD-ADCP instrument package (Fischer and Visbeck, 1993).	27
3.7	ADCP depth cells. ADCP measure average velocity over the depth range of the entire depth cell. (RDI, 1996).	28
3.8	ADCP single pings. The process of ADCP single pings (RDI, 1996).	28
4.1	Attenuation of LADCP shear spectrum in the finescale, which is compared to XCP shear spectrum. The spectra were estimated from the simultaneous XCP and LADCP profile pairs. The vertical resolution of XCP is higher than that of LADCP (Polzin et al., 2002).	33
4.2	ADCP tilt and depth map matching (RDI, 1996).	34

4.3	Spectral transfer function T_{theo} (Polzin et al. (2002) 2002) in dependence on the wavenumber β that computed with the settings used by Polzin et al. (black) and the setting used in the study (red) listed in Table 4.1.	36
5.1	Locations of hydrographic stations where the datasets were collected by Polzin et al. (2002) (black frame) and in this study (blue frame). Colors denote bathymetry.	37
5.2	Locations of LADCP-XCP pairs near the lesser Antilles in the western tropical Atlantic. Numbers correspond to stations of XCPs (black solid dot) and LADCPs (red hollow circle) profiles which are used in this study. Colors denote bathymetry.	39
5.3	Comparison between raw XCP (black) and LADCP (red) u (left) and v (right) velocity profile pair (XCP at station No.1 and LADCP at No.10).	40
5.4	Comparison between corrected XCP (black) and LADCP (red) u (top) and v (bottom) velocity profile pairs. Numbers along the upper axis are rms velocity differences between the two profiles. Numbers along the bottom axis are the station numbers of XCP and LADCP respectively. XCP profiles have been linearly stretched and offset to minimize the rms velocity difference between the profile pairs.	42
5.5	North velocity spectra (left), east velocity spectra (middle) and rotation frequency spectra (right) of the XCP profiles in the depth range from 220 m to 1220 m. The spikes appear in every north velocity spectra at the wavelength about 25 m. But the wavelength is varying with different XCP probes. There are no spikes in the east velocity spectrum. The spikes in the rotation frequency spectra are observed at the same vertical wavenumbers as the corresponding north velocity spectra. Columns: the corresponding spectra 1-7.	44
5.6	Coherence spectrum of XCP-LADCP velocity profiles. The coherence between XCP and LADCP velocity profiles form the depth range 220 m – 1220 m.	46
5.7	Vertical shear spectra of XCP (black) at station No. 1 and LADCP (red) at station No. 10. The corresponding transferred LADCP spectrum is the magenta curve. The GM model spectrum is the blue dotted curve. The same legend is used from Fig. 5.7 to Fig. 5.13. There are differences in the energy level between the XCP shear spectrum and LADCP shear spectrum.	50
5.8	Vertical shear spectra of XCP (black) at station No. 2 and LADCP (red) at station No. 10. The difference in the energy levels is similar as in Fig 5.7.	50

5.9	Vertical shear spectra of XCP (black) at station No. 3 and LADCP (red) at station No. 11.	51
5.10	Vertical shear spectra of XCP (black) at station No. 6 and LADCP (red) at station No. 16.	51
5.11	Vertical shear spectra of XCP (black) at station No. 7 and LADCP (red) at station No. 16.	52
5.12	Vertical shear spectra of XCP (black) at station No. 8 and LADCP (red) at station No. 17.	52
5.13	Vertical shear spectra of XCP (black) at station No. 9 and LADCP (red) at station No. 17.	53
5.14	Averaged vertical wavenumber shear spectra scaled by buoyancy frequency for the depth range 220 m – 1220 m. XCP shear spectra (black) are converted from velocity spectra. LADCP shear spectra (red) are estimated from LADCP shear profiles. The transferred LADCP shear spectra (magenta) are computed with the spectral transfer function of Polzin et al (Eq. (4.5)). The blue dotted curve is the GM model spectrum	54
5.15	Averaged vertical wavenumber shear spectra that are computed with shear spectra in Fig. 5.9-Fig. 5.13. The spectrum pairs in Fig. 5.7 and Fig. 5.8 are removed, when the averaged shear spectra are calculated.	54
5.16	Averaged strain spectrum (green). The strain spectra are computed with the method introduced in the section 2.2.4. There is no spike in the averaged strain spectrum. The energy level of strain spectra is lower than the averaged shear spectra of the XCP and LADCP profiles by a factor about 3.	55
5.17	Scatterplots of eddy diffusivities for each profile. The XCP inferred eddy diffusivities are larger than LADCP inferred eddy diffusivities, but most of them lie within a factor of 4. The numbers in the legend are the station numbers of XCP (left) and LADCP (right).	56
5.18	Rotated current sections from LADCP measurements. Locations of the two sections are depicted in Fig. 5.2. Velocities are positive in eastely directions, which perpendicular to the sections. Contours denote zero velocity. Top: section with the LADCP stations from No. 8 to No. 15. Bottom: Section with the LADCP stations from No. 23 to No. 15.	58

List of Tables

4.1	The setting for the model spectral transfer function used by Polzin et al. and used in this study.	36
5.1	Comparison between LADCP instrument design employed by Polzin et al. (2002) and that used in the caribinflow cruise. . . .	38
5.2	The vertical and horizontal offsets used to correct the XCP profiles in comparison to LADCP profiles.	41

1

Introduction

Although vertical mixing in the interior ocean is small, it has raised the interest of the oceanographic community due to its importance for the oceanic large scale circulation. It was a challenge to measure the mixing in the ocean in time and space. Oceanographers were faced with the sampling problems.

For the past fifteen years, a parametric model was built and developed to calculate the vertical mixing (McComas and Müller 1981; Henyey et al., 1986; Gregg, 1989 and Polzin et al., 1995). The parameterization was built on the association between the vertical mixing and the internal wave field. The internal wave field can be expressed by the spectra of current profiles. Hence, the vertical mixing rates can be determined by the measurement of current profiles. However, it is difficult to obtain full-water-depth current profiles. The lowered acoustic Doppler current profile (LADCP) is an economic and practical current profiler that can measure the horizontal current velocity in the abyssal ocean. The existing LADCP datasets over the wider dynamic regimes give the opportunity to establish basin-wide vertical mixing levels in the ocean interior.

Attenuation is observed in the wave spectra estimated from LADCP profiles. It occurs in the finescale, which denotes the wavelength region from 10 m to 100 m. This would provide less accurate estimates of the vertical mixing rates. Polzin et al. (2002) analyzed the reasons for the attenuation in the spectrum and built a model transfer function to correct the LADCP spectra in the finescale. The reproduced LADCP spectra are compared with the other spectra that are estimated from expendable current profiler (XCP) profiles. The XCPs have higher vertical resolution and provided better information in the finescale of the wave spectra. But the depth range of XCPs is limited to about 1500 m, therefore they can not be used to estimate the vertical mixing in the abyssal ocean. The corrected LADCP spectra estimated by Polzin et al. resembled the XCP spectra. They used the transferred LADCP spectra and XCP spectra to calculate mixing rates and obtained comparable results. Therefore the model spectral transfer function can be used to estimate the vertical mixing rates.

But since the model was built, the LADCP has been developed in the instrument design and processing method. Thus the model should be validated with our own data.

In this study, the data were collected during the cruise CARIBINFLOW in

April 2003 near the lesser Antilles in the western tropical Atlantic. Two self-contained 300 kHz ADCPs manufactured by RD Instrument and XCPs manufactured by Sippican were employed to measure the current profiles. Using these data, the model spectral transfer function of Polzin et al. (2002) is validated with the same method that is used by Polzin et al. (2002). The reproduced LADCP spectra that are corrected by the model spectral transfer function of Polzin et al. (2002) are compared with XCP spectra. The mixing rates are calculated from the reproduced LADCP spectra and XCP spectra, respectively.

The spectral densities of the LADCP spectra are enhanced in the finescale, when the model of Polzin et al. (2002) is applied. Then the corrected LADCP spectra resemble XCP spectra. The mixing rates calculated from the corrected LADCP spectra are comparable to the mixing rates computed from the XCP spectra. Thus, it is validated, that the model spectral transfer function of Polzin et al. (2002) is suitable to our data, and it can be used to study vertical mixing with the LADCP data.

The importance of determining mixing and the method to calculate the mixing rates are discussed in the chapter 2; the two different current profilers (XCP and LADCP) are introduced in chapter 3; The model spectral transfer function is presented in chapter 4; the results of validation of the model are given in chapter 5; and the last chapter is the summary and conclusion.

2

Mixing and Internal Waves

2.1 Mixing

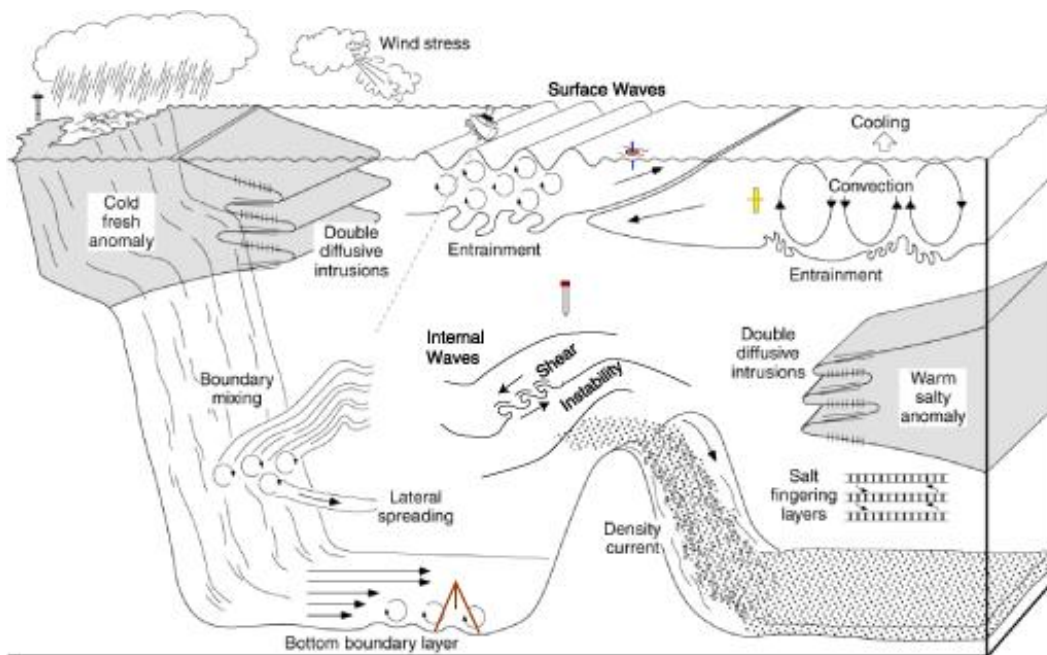


Figure 2.1: Various processes which are associated with mixing in the ocean. Figure taken from the web site of the University of Washington.

Mixing occurs everywhere in the ocean as depicted in Fig. 2.1. It can be divided into boundary and open water processes. Boundary mixing occurs at the upper boundary or the surface mixed layer in the ocean, and also in the bottom boundary layer (BBL) in the deep ocean. The processes in the upper layers of the ocean are driven by the wind and surface buoyancy fluxes, while the turbulent mixing in BBL is induced by interaction of currents with the roughness of the topography.

Mixing away from the boundaries in the ocean interior is difficult to study, because the oceanographers were faced by the sampling problem both in time

and space until few years ago. However, great progress has been made in understanding the sources of energy for mixing, the mechanisms and the rates. They will be briefly discussed in subsection 2.1.2 and in section 2.2.5.

Turbulence in the ocean leads to mixing. According to the direction of the turbulent motion, mixing can also be classified in two basic classes: isopycnal mixing and diapycnal mixing. Sometimes these two basic classes are also named as horizontal mixing and vertical mixing with little differences. The direction of diapycnal mixing is perpendicular to the isopycnal surfaces, the constant-density surfaces, while the the direction of vertical mixing is perpendicular to the sea level.

Horizontal mixing is much larger than vertical mixing, because vertical displacement must work against the buoyancy force due to the stable stratification of the ocean, but vertical mixing is more important for the ocean.

2.1.1 The Importance of Vertical Mixing

By means of the vertical mixing, kinetic energy from the large scale motion is converted into potential energy. This process counteracts the vertical advection, and then maintains the stratification in the ocean. Moreover, the deep mixing is important to the strength and state of the thermohaline circulation. The simplest view of the thermohaline circulation of the oceans is that cold and dense water sinks at high latitudes then spreads equatorward and rise up to the surface where the water could be warmed and made lighter again by solar heating. Vertical mixing prevents the realization of such oceanic structure. This simultaneously leads to a diffuse thermocline, an increased meridional overturning rate, and increased meridional heat flux (Fig. 2.2). Hence, determining vertical mixing in the world ocean is an important step toward closing the thermohaline circulation and modeling large-scale ocean dynamics correctly (Munk and Wunsch 1998).

2.1.2 Estimated and Measured Vertical Mixing

When discussing the mixing rate, an important parameter to quantify mixing is eddy diffusivity, namely the turbulent mixing coefficient, which is the exchange coefficient for the diffusion of a conservative property (heat or salt or momentum) by eddies in a turbulent flow.

Average Vertical Mixing

It is observed that the ocean has a pycnocline almost everywhere, and the pycnocline below the surface mixed layer dose not change even over decades. Such a steady-state pycnocline is described by Munk (1966) with vertical advection-diffusion balance as:

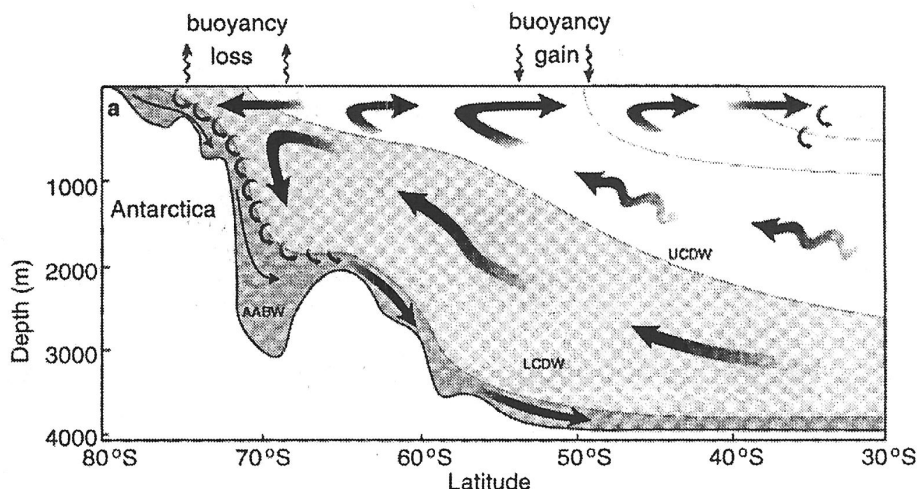


Figure 2.2: Schematic showing the meridional overturning circulation in the Southern Ocean (Gargett 1998).

$$w \frac{\partial \rho}{\partial z} = K_\rho \frac{\partial^2 \rho}{\partial z^2} \quad (2.1)$$

where K_ρ is the eddy diffusivity for density, w is a mean vertical velocity, and ρ is density as a function of depth in the pycnocline. Munk assumed uniform vertical velocity $w = 0.5 - 1 \text{ cm day}^{-1}$ which is inferred from deep-water formation rates. This balance model implies an averaged diapycnal eddy diffusivity, $K_\rho \simeq 10^{-4} \text{ m}^2 \text{ s}^{-1}$.

Measured Vertical Mixing

Vertical mixing can be observed directly by microstructure measurements and tracer release experiments. Microstructure measurements (e.g. Osborn and Cox 1972; Gregg 1987; Toole et al. 1994) find eddy diffusivities $K_\rho \simeq 0.1 \times 10^{-4} \text{ m}^2 \text{ s}^{-1}$ over abyssal plains.

This low value is confirmed by tracer release experiment (e.g. Ledwell et al. 1998). In this experiment sulphur hexafluoride (SF_6) was injected as tracer in the Atlantic near 26°N , 29°W to obtain a diapycnal eddy diffusivity of $K_\rho = 1.2 \pm 0.2 \times 10^{-5} \text{ m}^2 \text{ s}^{-1}$.

The large discrepancy between Munk's calculation of the mean eddy diffusivity for vertical mixing and the observed values in the open ocean has been explained by the later studies (Polzin and Firing 1997; Toole et al. 1997; Mauritzen et al. 2002). These studies used different measurement techniques and suggested that rather than being uniformly distributed, ocean mixing might be concentrated over rough or steeply sloping topography (Fig. 2.3).

Nevertheless, the eddy diffusivity remains undersampled by microstructure measurements and tracer releaser experiments. For the microstructure mea-

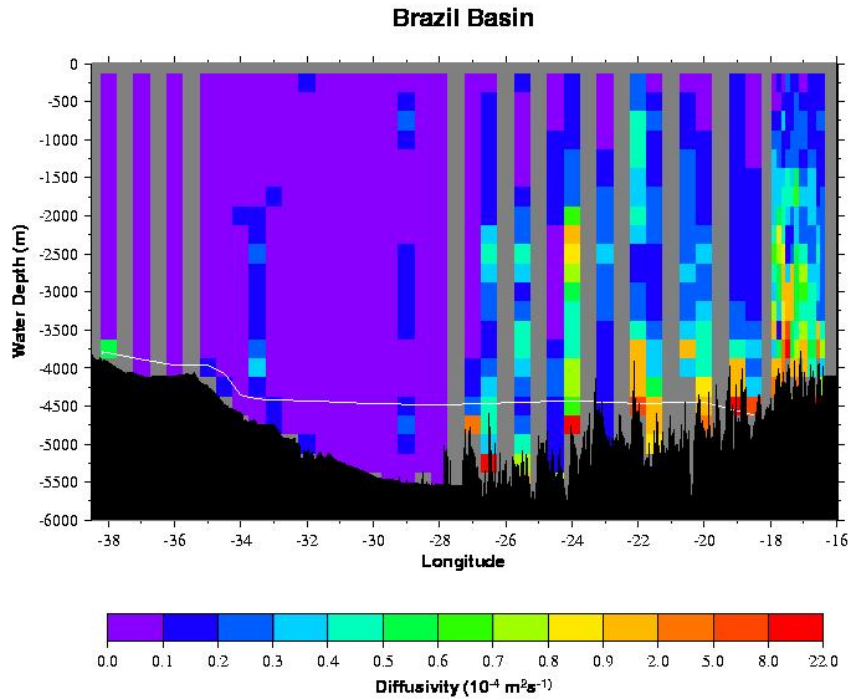


Figure 2.3: A section of turbulent diffusivity across the Brazil Basin. The diffusivity estimates were made using observation of velocity measurements which were averaged into 200 m vertical bins. (Polzin and Firing, 1997).

measurements, it is required that the probes are able to measure temperature and salinity with a spatial resolution of few centimeters (Gregg and Kunze, 1991), because the spatial scale of the turbulent mixing is from large scale to few centimeters. For trace release experiment, the time durations are usually few months or even longer. Therefore another method is required to estimate the eddy diffusivity.

It has been argued that elevated mixing rates are involved with the interactions of internal tides and internal waves with topographic roughness. Therefore, McComas and Müller (1981) and Henyey et al. (1986) developed a turbulence-production parameterization, which is based on the energy transfer caused by the internal wave-wave interactions. These parametric models were further improved by Gregg (1989) and Polzin et al. (1995) to estimate the eddy diffusivity. The models employ the velocity profiles which were collected with a wider coverage of abyssal waters. Hence, LADCP datasets give the opportunity to establish basin-wide abyssal mixing levels. In the following section, the overview of the internal wave and the parametric model will be briefly introduced.

2.2 Internal waves

2.2.1 The Internal Wave Field

Internal waves occur at the interface between any two layers of ocean water of differing densities and propagate in the interior ocean. In turn, internal waves cause simultaneous oscillations in the velocity and density field. Internal wave breaking furthermore results in vertical mixing.

Internal waves travel in the same manor as surface waves, but at much slower speeds if they have comparable amplitude. Oscillations are more easily set up at the interface than at the sea surfaces, because the density difference between two ocean layers is typically much less than the density difference between water and air. Hence, less energy is required to generate internal waves than surface waves of similar amplitude.

As surfaces waves, internal waves can be assumed as linear waves. It is reasonable, because the the amplitude of internal waves at the interface is infinitely small so the interface is almost exactly a plan. According to linear theory, internal waves must obey the dispersion relation

$$\frac{N^2(z) - \omega^2}{\omega^2 - f^2} = \left(\frac{\beta}{\alpha}\right)^2 \quad (2.2)$$

where α and β are the horizontal and vertical wavenumber, respectively. According to Eq. (2.2), the intrinsic frequency of the internal waves ω falls in the range between the buoyancy frequency N and the Coriolis frequency f . The Coriolis frequency is associated with the rotation of the earth as $f = 2\Omega \sin \varphi$, where $\Omega = 7.292 \times 10^{-5} \text{ s}$ is the rotation rate of earth and φ is latitude.

Buoyancy frequency N is a fundamental variable in the dynamics of stratified flow. The frequency quantifies the importance of stability. It is expressed by the density gradient as

$$N^2 = -\frac{g}{\bar{\rho}} \frac{\partial \rho}{\partial z} \quad (2.3)$$

with density ρ and gravitational acceleration g . Typical values of N are a few cycles per hour.

Unlike surface waves, internal waves can not be measured by satellites. A good way to visualize internal waves is to observe the fluctuations in oceanographic records. Oceanographers find it convenient to express the wave fields as spectrum which gives the distribution of wave energy among different wavenumbers/frequencies. Note, that in oceanography the term “time series” can be applied to both temporal and spatial data series; methods which apply in the time domain also apply in the space domain. Hence, the term frequency and wavenumber (the formal transform of the time and spatial series, respectively) are used interchangeably.

2.2.2 Wave Spectrum

According to Fourier Theory, any wave function $y(t)$ can be represented over the interval $0 \leq t \leq T$ as the sum of an infinite series of complex exponential functions with harmonic wave frequencies $f_p = p/T$ as:

$$y(t) = \sum_{p=-\infty}^{\infty} Y_k \exp^{i2\pi f_p t} \quad (2.4)$$

where

$$Y_p = \frac{1}{T} \int_0^T y(t) \exp^{-i2\pi f_p t} dt, \quad p = 0, 1, 2, \dots \quad (2.5)$$

Y_p is called the Fourier transform.

The spectrum is:

$$S(f_p) = Y_p Y_p^* \quad (2.6)$$

where Y_n^* is the complex conjugate of Y_n .

Most oceanographic time or space series are digital data. Therefore, instead of the continuous function $y(t)$, an infinitely long time series $y(t_n) = y_n$ should be considered. The data are sampled at equally spaced time increments $t_n = n\Delta t$, where Δt is the sampling interval and n is an integer, which is limited in the range $1 \leq n \leq N$, where N ($T = N\Delta t$) is the total number when data values in the time series. The discrete Fourier transform is:

$$Y_k = \Delta t \sum_{n=1}^N y_n \exp^{-i2\pi f_k n \Delta t} \quad (2.7)$$

where the frequencies f_k are

$$f_k = k/N\Delta t; \quad k = 0, \dots, N \quad (2.8)$$

The discrete Fourier transform is speeded up by fast Fourier transform (FFT) that is commonly used by the computer.

In this study, the spectrum S is expressed in terms of power spectral density (PSD). Here, power is defined as energy per unit time. One side power spectral density G_{yy} computed from FFT is:

$$G_{yy} = \frac{2}{N\Delta t} |Y_k(f_k)|^2 \quad (2.9)$$

Vector time series such as horizontal velocity profiles and vertical shear of the horizontal velocity profiles (see section 2.2.4) are used to calculate the spectra in this study. Spectral analysis for vector is applied to the combined series of components and the results expressed as a complex function. For example, the horizontal velocity profile can be represented as

$$w(z) = u(z) + iv(z) \quad (2.10)$$

where real part $u(z)$ is the eastward velocity and imaginary part $v(z)$ is the northward velocity.

The discrete Fourier transform for this two dimensional vector is

$$W(k_p) = U(k_p) + iV(k_p) \quad (2.11)$$

$$= \Delta z \sum_{n=1}^N [u(z) + iv(z)] \exp^{-i2\pi k_p n \Delta z} \quad (2.12)$$

where $k_p = p/N\Delta z$; $p = 1, \dots, N$; and where $U(k_p)$ and $V(k_p)$ are the Fourier transform of $u(z)$ and $v(z)$, respectively.

The spectral density function is given in terms of one-side spectrum as

$$G_{ww}(k'_p) = \frac{2}{N\Delta t} |W(k'_p)|^2 \quad (2.13)$$

$$= \frac{2}{N\Delta t} \{ [W_R(k'_p)]^2 + [W_I(k'_p)]^2 \} \quad (2.14)$$

$$= \frac{2}{N\Delta t} \{ [U_R(k'_p) - V_I(k'_p)]^2 + [U_I(k'_p) + V_R(k'_p)]^2 \} \quad (2.15)$$

where $k'_p = p/N'\Delta t$; $p = 0, 1, \dots, N'/2$ is the vertical wavenumbers for the spectrum of horizontal velocity profile and to FFT analysis for complex series, $N' = 2q$ (positive integer q); and where the subscripts R and I stand the real and imaginary parts of the given Fourier components.

2.2.3 The Garrett and Munk Model

Despite the large temporal and spatial variabilities of the internal wave field, the shape of observed wavenumber/frequency spectra seems to be remarkably universal. This led Garrett and Munk (1972) to the derivation of a semi-empirical universal model on the basis of linear theory and synthesis of existing data that describe the observed distribution of internal wave energy in wavenumber and frequency space. The basic assumptions for the model were horizontal isotropy (waves coming in from all horizontal directions equally) and vertical symmetry (as many waves are propagating downward as upward). The resulting model spectrum was presented as an equivalent continuum spectrum, without any spectral lines.

Most of the detail features of this spectrum were confirmed by the trimoored (three-dimensional moored) internal wave experiment IWEX (Müller et al., 1978). The initial model was modified by Garrett and Munk (1972), Cairns and Williams 1976, Munk (1981) and Levine (2002), which are customarily referred to as the GM model. In this study, the version of GM76 (Cairns and Williams, 1976) is employed.

The GM 76 model spectrum of horizontal velocity is a function of wavenumber β in radians per meter as

$$\Phi_u = \frac{3Eb^3N_0^2}{2j * \pi} \frac{1}{(1 + \beta/\beta_*)^2} \quad (2.16)$$

where $E = 6.3 \times 10^{-5}$ is the dimensionless energy level, $b = 1300$ m is the scale depth of the thermocline, and $N_0 = 0.00524 \text{ rad s}^{-1}$ is the reference buoyancy frequency corresponding to 3 cycles per hour.

It should be noted that the GM spectrum is dependent on the stratification, as the spectral energy level of internal wave fields depend on stratification. Therefore, the comparison between data sets from different physical environments in the ocean is allowed.

2.2.4 Shear and Strain Spectra

Instead of energy spectra of the the wave field, the spectra of shear and strain are more generally used. The vertical shear is the vertical variation of the horizontal current velocity as

$$S_z = \frac{\partial u}{\partial z} + i \frac{\partial v}{\partial z} \quad (2.17)$$

and vertical strain is the vertical variation of the vertical displacement of isopycnals (η) as

$$\lambda_z = \partial \eta / \partial z. \quad (2.18)$$

A composite spectrum of the vertical shear of horizontal velocity in the ocean from three different microstructure experiments was presented by Gargett et al. (1981) (Fig.2.4).

The spectrum is white (the spectral constituents have near-equal amplitude through the frequency range) at vertical wavelengths larger than 10 m. In the range of wavelengths between 10 m and 1 m, the spectrum is red (the spectral density decreases with increasing wavenumber) with a slope roughly about -1 . In the range of wavelength below 1 m, the spectrum becomes turbulent and shows a Gaussian shape.

There are two methods to estimate shear spectrum. It can be estimated from shear profile using the method of Fourier analysis (as mentioned in section 2.2.2). It can also be converted form the velocity spectrum as

$$\Phi_s(\beta) = \beta^2 \Phi_u(\beta) \quad (2.19)$$

where β is vertical wavenumber in radians per meter. The velocity spectrum is computed from velocity profiles by means of Fourier transform.

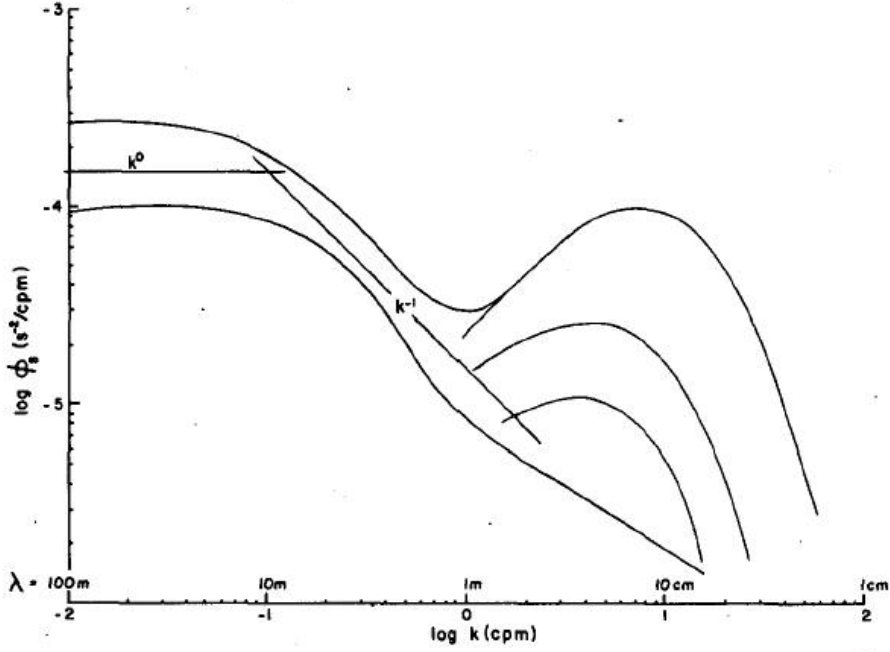


Figure 2.4: A composite spectrum of vertical shear of horizontal velocity (Gargett et al., 1981).

According to Eq. (2.18), strain is defined as the vertical derivative of isopycnal displacement and requires quantifying departures from a time-mean density profile. But estimates of the time mean are not available from data obtained as part of a hydrographic section. Instead, it is assumed that large vertical length scales in the density profiles represent the time mean and that all small vertical length scales represent the internal wave field. Under this assumption the strain can be estimated from N^2 variability as

$$\lambda_z = \frac{N^2 - \overline{N^2}}{\overline{N^2}} \quad (2.20)$$

where $\overline{N^2}$ is estimated as linear fits to the specific volume anomaly depth profiles using the adiabatic leveling method of Bray and Fofonoff (1981) over approximately 400 m. The resulting strain estimate λ_z are then Fourier transformed to obtain the strain spectrum.

Since both shear and strain are physical quantities referred to fluctuation in the ocean, the shear and strain spectra should be similar and comparable according to GM model. The GM76 model for shear and strain are

$$\Phi_s(\beta) = \beta^2 \Phi_u(\beta) \quad (2.21)$$

$$\Phi_\lambda(\beta) = \beta^2 \Phi_\eta(\beta) \quad (2.22)$$

where Φ_u is the GM model spectrum of velocity u (Eq. (2.16)) and Φ_η is the GM model spectrum of isopycnal displacement η .

2.2.5 Inferring Eddy Diffusivity

Based around the GM spectrum, two dynamical models (McComas and Müller, 1981 and Henyey et al., 1986) were developed to explain the energy transfer processes which result in the universal spectral distribution of the internal wave field. In spite of the differences in the theory behind the models, they give rather similar answers. The models also provide the parameterizations for the turbulent dissipation rate ϵ depending on energy E , buoyancy frequency N and Coriolis parameter f .

Gregg (1989) indicates furthermore that the energy density of the internal wave spectrum E_{IW} can be associated to the vertical shear variance, $\langle S_z^2 \rangle$, (wavenumber $<$ cut-off wavenumber, k_c) in relation to the appropriate values from GM model as

$$E_{IW}/E_{GW} = \langle S_z^2 \rangle / \langle S_{GM}^2 \rangle \quad (2.23)$$

Polzin et al. (1995) modified the parametric model in addition with a shear/strain ratio correction, $f(R_w)$, in which R_w is a ratio of vertical shear to vertical strain as

$$R_w = \frac{\Phi_s(\beta)}{N^2 \Phi_\lambda(\beta)} = \frac{(N^2 - w^2)(w^2 + f^2)}{N^2(w^2 - f^2)} \quad (2.24)$$

where Φ_s and Φ_λ are the power spectral density (PSD) of shear and strain in dependence on the analytic wavenumber $\beta (= 2\pi k)$. Notice that for the GM model the shear to strain ratio $R_{GM} = 3N^2$ (Kunze et al., 2002).

The shear/strain ratio correction

$$f(R_w) = \frac{R_w + 1}{R_{GM} + 1} \sqrt{\frac{R_{GM}^3 [1 - R_w + \sqrt{(R_w - 1)^2 + 8R_w f^2 / N^2}]}{R_w^3 [1 - R_{GM} + \sqrt{(R_{GM}^2 - 1) + 8R_{GM} f^2 / N^2}]}]} \quad (2.25)$$

brought the estimates into better agreement, however, this correction term is usually set to one, if the internal wave spectrum does not differ too much from the GM spectrum (Polzin et al., 1995).

Finally, the resulting parameterization for the turbulent kinetic energy dissipation rate is

$$\epsilon = \epsilon_0 \frac{N^2}{N_0^2} \frac{\langle S_z^2 \rangle^2}{\langle S_{GM}^2 \rangle^2} f(R_w) \quad (2.26)$$

Using the dissipation rate ϵ , Osborn (1980) inferred the turbulent eddy diffusivity, K_ρ , from the relation

$$K_\rho = \frac{\gamma \epsilon}{N^2} \quad (2.27)$$

with the mixing efficiency $\gamma(\leq 0.2)$. The mixing efficiency is usually set at its maximum value of $\gamma = 0.2$ in stratified waters.

With this method, dissipation rate ϵ and eddy diffusivity k_ρ are estimated from vertical shear spectrum, which are determined from the shear or horizontal velocity profile. Hence, two different instruments used to provide the velocity profile are discussed in the following chapter.

3

Measurements

Two different current profiles are introduced in this chapter. The expendable current profiler (XCP) is introduced in the section 3.1, and the lowered acoustic Doppler current profiles (LADCP) is introduced in the section 3.2. The operation theories of these two current profiles are described. The accuracy and the performance of the XCPs are discussed. The data processing method of the LADCP are described in the LADCP section. At the end of this chapter, the CTD instrument is briefly introduced.

3.1 Expendable Current Profiler

The expendable current profiler (XCP) measures ocean velocity and temperature from the surface to a depth about 1500 m. XCPs have been manufactured and developed since the 1970's. The XCP (Fig. 3.1) is designed to be launched by hand over the side of a moving ship. The measured signals are transmitted and then received by data acquisition equipment on the ship.

They have been used in a variety of oceanographic programs over the world. One significant advantage of XCPs is the high vertical resolution. The other advantages of XCPs are that they can be deployed over a large range of latitudes ranging from the equator to about 85° N or 85° S and from any sort of platform: ship, aircraft, ice, etc. Moreover, XCPs can be launched in any weather conditions, including hurricanes. But XCPs are expendable and expensive and the depth range of the XCP is just from the sea surface to the depth of about 1500 m. Therefore, it is not convenient to use XCPs extensively throughout the ocean; and it is impossible to estimate the eddy diffusivities in the abyssal ocean by means of XCP profiles.

In this section the operation theory is given at first, then the instrumentation of XCPs is introduced, finally the performance of XCP is discussed.

3.1.1 Theory of Operation

Velocity determination of XCPs are based on the principles of electromagnetic induction that govern the weak electric currents that are induced by the motion of electrically conducting layers of seawater through the Earth's magnetic field

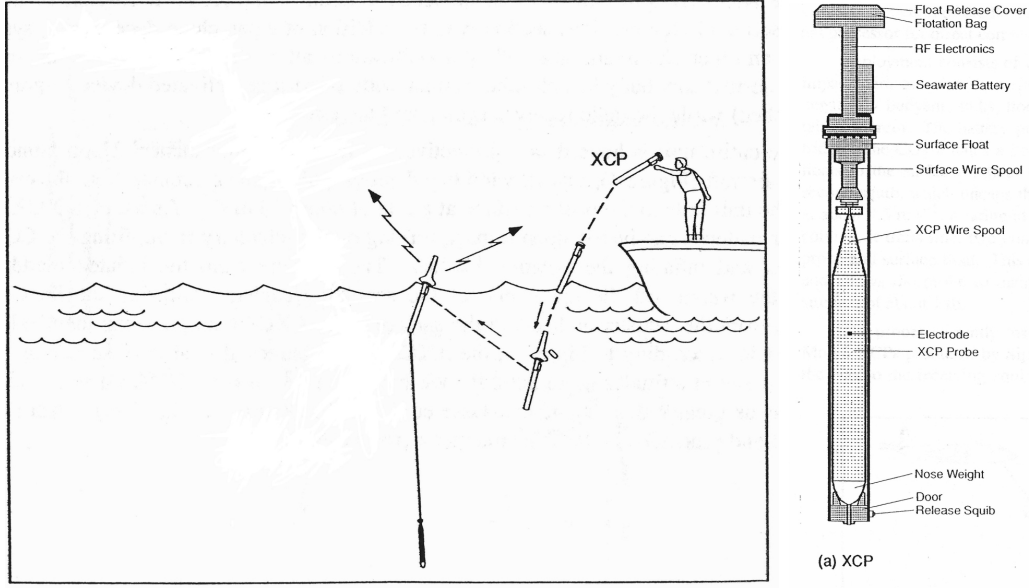


Figure 3.1: Left: XCP launch sequence from underway vessel. Right: XCP schematic (Sanford et al., 1993).

(Sanford et al., 1981). The magnitude of the electric current is related to the velocity of the conductor, its conductivity, and the strength of the magnetic field. The XCP determines the current velocity by measuring the voltage between horizontally spaced electrodes falling through the water column. Sanford (1982) gave the equations for the east and north velocities as:

$$u = \bar{u} + \frac{\delta\phi_n}{F_z l (1 + C_1)} \quad (3.1)$$

$$v = \bar{v} - \frac{\delta\phi_e}{F_z l (1 + C_1)} + w \frac{F_h (1 + C_2)}{F_z (1 + C_1)} \quad (3.2)$$

where $\delta\phi_n$ and $\delta\phi_e$ are the northward and eastward electric potential differences estimated from the voltage drop between electrodes and then sensed by the XCP, \bar{u} and \bar{v} are the east and north components of the vertically averaged horizontal velocity, F_h and F_z are the Earth's horizontal and vertical magnetic fields, l is the electrode separation, C_1 and C_2 are XCP coefficients depending on the shape of the probe and w is the vertical fall speed of the probe relative to the water. Thus, XCP measure only the relative velocities.

The depth of the XCP is estimated as a quadratic function of the fall time:

$$z = z_0 + z_1 t + z_2 t^2 \quad (3.3)$$

where z is the depth (positive downward from the surface) and t is the elapsed fall time. The coefficients z_i of the quadratic polynomial are determined empirically. In addition, the vertical velocity of the XCP, w , in Eq. (3.2) is obtained

by the derivation of the depth equation:

$$w = z_1 + 2z_2t \quad (3.4)$$

3.1.2 Instrumentation

The entire XCP system consists of a free-falling sensor probe, a surface float with a radio transmitter, and wire connecting the probe and the transmitter (Fig. 3.1).

The probe is projectile-shaped, with a cruciform tail and ring shroud; it contains electrodes, a compass coil, electronics, batteries, a thermistor, and wire-spooling components (Fig. 3.1). The voltage drop between two separated electrodes is measured to estimate the horizontal velocity. Determination of the two horizontal components of velocity is enabled by a compass coil wound coaxially over the electrode tubes. As the probe falls, the compass-coil signal is used to determine the location of magnetic north once per revolution. A thermistor mounted within a flow tube on the probe provides a continuous vertical temperature profile. The motionally induced voltage, sensed between the electrodes, and the compass coil voltage are amplified and converted to frequency separately. Frequency-modulated (FM) signals are summed together for transmission up the wire connecting the probe to the surface float and telemetered to the ship via a radio frequency (RF) transmitter to a very high frequency (VHF) radio receiver on the ship. The output of the RF receiver is amplified, demodulated, and digitized by the signal processor for direct computer storage. The battery provides power to fire a squib which punctures a CO₂ cartridge. The CO₂ inflates a flotation bladder, and the system, buoyed up by the bladder, floats to the surface. Few seconds later, a timer, activated at battery power-up, fires a second squib, which uncaps the bottom of the probe's launch tube, the probe then falls rotating downward. As it drops through the water column, it trails fine wire which deploys from spools on both the probe and surface float. This method of deployment eliminates an increasing drag force and allows the probe to maintain a uniform descent speed.

3.1.3 Accuracy and Performance of XCP

The performance of XCP near the geomagnetic equator and poles degrades owing to the change of Earth's magnetic field. It can be explained by the horizontal velocity equations (Eq. (3.1) and Eq. (3.2)). As one approaches the magnetic equator, F_z begins to vanish. This cause terms scaled by $1/F_z$ and F_h/F_z to appear larger near magnetic equator than at mid-latitudes; thus differences between the assumed and actual fall rate, i.e. w and electrode/electronic noise contributions will be amplified near the magnetic equator. In contrast, at very high latitudes, as F_h decreased the compass coil signal will become increasingly small, until it can no longer be used. It is observed that the XCP does

not perform well within 1° to 2° of the magnetic equator and within 5° of the magnetic pole.

The other important element to generate errors is the vertical fall rate of the probe, w . It is used in the computation of the geomagnetic north velocity v (Eq. (3.2)). It is testified, that if the variation of the w exceeds a few centimeters per second, this error in the v velocity may become noticeable. The effect of fall rate variations on north velocity was found during analysis of XCP data from the Gulf of Cadiz Expedition (Sanford, 1982). A “spike” was observed in the north (v) velocity spectrum near the vertical number 20 m, that did not appear in the east (u) velocity spectrum. A spike at the same vertical number appeared in the XCP rotation frequency (f_{rot}) spectrum. The rotation frequency profiles are recorded, when the XCPs fall rotating downward. The vertical number, at which the spike appears is varies with different depth of the velocity profile and for different probes for unknown reason. The source of the oscillations of v and f_{rot} is explained by a hypothesis: The wire coming off the spool induces a (somewhat) periodic upward force, causing the probe to slow and speed its descent with the same periodicity. The fall speed w changes, in turn, cause a change in f_{rot} , because of the probe’s moment of inertia.

3.2 Lowered Acoustic Doppler Current Profilers

Acoustic Doppler current profilers (ADCPs) measure the velocity by means of Doppler Effect. They can be attached to a CTD package (depicted in Fig. 3.2) and lowered into the deep ocean and retrieved back to the ship (depicted in Fig. 3.6). In this way, Lowered acoustic Doppler current profilers (LADCP) provide full-water-depth velocity profiles. The LADCP operation is simple and ADCPs are very economic instruments. Therefore, LADCPs are widely used and provide current profiles over a wider coverage in the deep ocean.

Two broadband 300 kHz ADCPs with 20° beam angle manufactured by RD Instruments (RDI, 1996) are used in this study.

In this section, the theory of Doppler effect is briefly reviewed at first, then the method about the achievement of three-dimensional current velocity vectors and the way to estimate the the velocity profile are introduced, finally the two different methods to process the raw LADCP data are described.

3.2.1 Doppler Effect

ADCPs measure the velocity on the basis of the Doppler Effect. The acoustic Doppler effect is a shift (called as Doppler shift) in frequency of a sound wave due to the relative movement of the source or the observer. ADCPs use the Doppler effect by transmitting sound at a fixed frequency and listening



Figure 3.2: A photo of CTD-ADCP instrument package. The two yellow ADCPs are attached to rosette frames in opposite direction (one upward and the other downward). Photo is given by O. Bislich.

to echoes returning from sound scatterer (small particles or plankton in the water). The process is depicted in the Fig. 3.3.

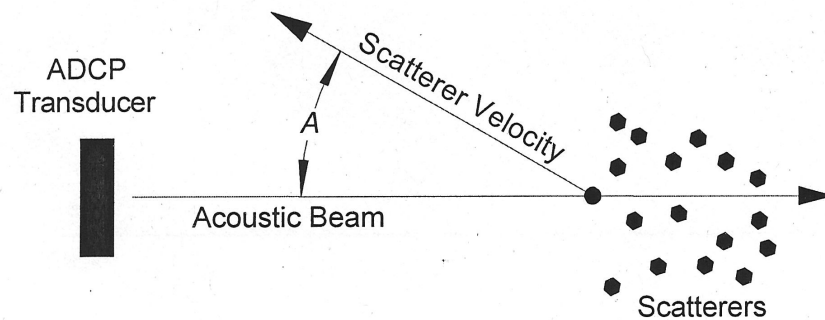


Figure 3.3: Schematic drawing depicting the measurement of relative velocity on the basis of acoustic Doppler effect. The ADCP measures only the velocity component parallel to the acoustic beams (RDI, 1996).

The equation for the Doppler shift in this situation is

$$F_d = 2F_s(V/C) \cos(\alpha) \quad (3.5)$$

where F_d is the Doppler shift frequency. F_s is the frequency of sound transmitted by ADCP. V is the relative velocity between the ADCP (i.e. CTD frame) and scatterer. C is the speed of sound. α is the angle between the relative velocity vector and the line between the ADCP and the scatterer. The Doppler shift is limited by the term $\cos(\alpha)$, because the Doppler shift only works in the direction between the sound source and receiver. Notice that the Doppler shift is doubled in the Eq. (3.5), because the ADCP is employed as both transducer and receiver, hence, the frequency is shifted by moving scatterer two times. Applying Eq. (3.5), ADCPs estimated the velocity by means of measuring the Doppler shift frequency.

3.2.2 Three-dimensional Current Velocity Vectors

According to Eq. (3.5), a single acoustic beam can only measure a single velocity component that is parallel to the beam. In order to obtain three velocity components (e.g. east, north and vertical components), ADCPs employ two pairs of acoustic beams, altogether four beams. One pair beams is shown in Fig. 3.4.

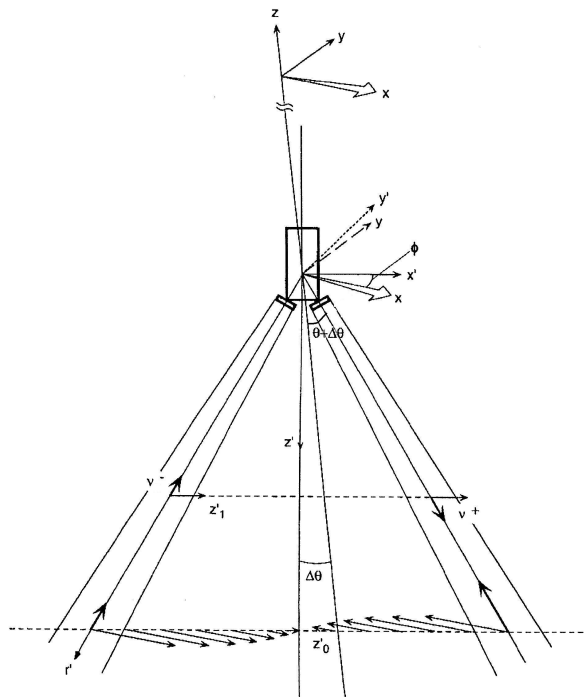


Figure 3.4: Schematic of the LADCP measurement geometry (Polzin et al., 2002).

Four acoustic beams typically slant at an angle, θ , ($\theta = 20^\circ$ to the ADCPs used in this study) from the vertical plane and spaced at 90° intervals (Janus configuration), depicted in Fig. 3.5.



Figure 3.5: ADCP sensor head. The red circles denote the 4 transducer faces (The Figure is taken from the website of the RDI).

Each pair of opposing slant velocities v^+ and v^- is combined to produce estimates of horizontal velocity

$$u_{\text{ADCP}} \text{ OR } v_{\text{ADCP}} = -\frac{v^+ + v^-}{2 \sin \theta} \quad (3.6)$$

and vertical velocity

$$w_{\text{ADCP}} = \frac{v^+ + v^-}{2 \cos \theta} \quad (3.7)$$

under the assumption that the flow field is horizontally uniform over the beam separation. Thus with two pairs of acoustic beams, ADCPs estimate two horizontal velocity components and two independent vertical velocities. Two horizontal velocities are orthogonal to each other. Horizontal velocity components are converted from ADCP coordinate system into Earth coordinates by means of heading data, which are measured by the compass of the ADCP. The difference between the independent estimates of vertical velocity is referred to as the error velocity and provides a consistency check whether the assumption of horizontal homogeneity is reasonable. The vertical component of ocean currents is a very small quantity ($\simeq 1 \text{ cm s}^{-1}$). The accuracy of velocity estimated by ADCPs is also in the order of about 1 cm s^{-1} . Hence, estimates of vertical velocity can rarely be used to infer the vertical component of the ocean currents.

3.2.3 Velocity Profile

The discussion so far has concerned the estimates of horizontal velocity vectors at one certain depth. The most important feature of ADCPs is their ability to measure current profiles. One acoustic pulse transmitted by ADCPs can propagate in the water to a certain range until the strength of echoes is largely reduced by sound absorption. This vertical depth range will be denoted as z'_{max} . Note that employing two ADCPs in a CTD package (Fig. 3.2) doubles the maximum of the vertical range.

ADCP divide the velocity profile into uniform segments called depth cells (or bins). The sign Δz_r denotes the length of the depth cell. The depth cells

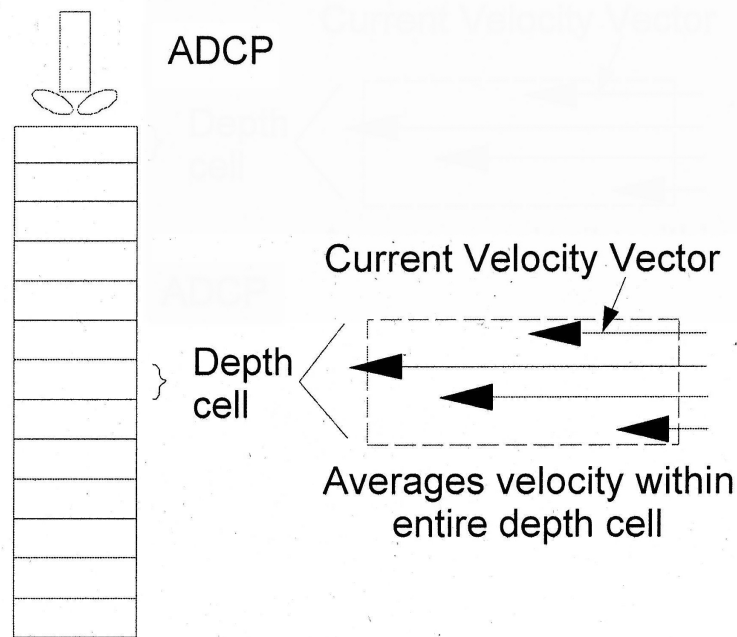


Figure 3.7: ADCP depth cells. ADCP measure average velocity over the depth range of the entire depth cell. (RDI, 1996).

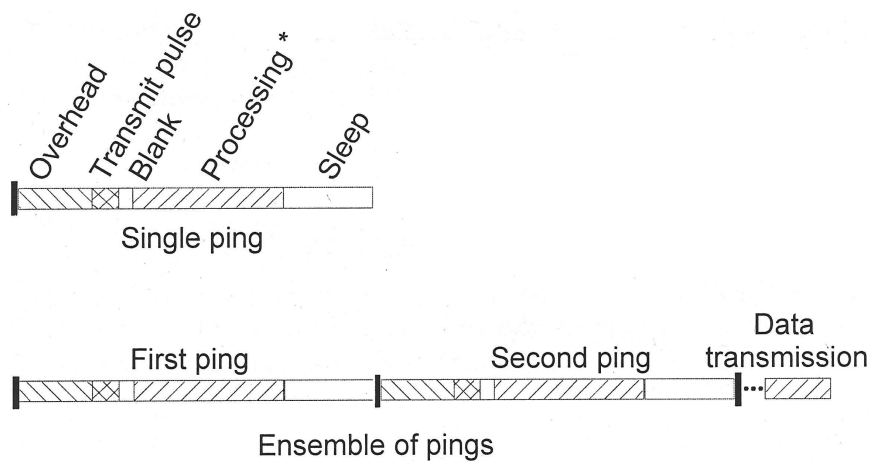


Figure 3.8: ADCP single pings. The process of ADCP single pings (RDI, 1996).

or immediately begins another data collection cycle. So far, the single-ping velocity profiles (individual ADCP profile) cover only a small depth range of the water column. LADCPs obtain successive overlapping velocity profiles by means of lowering ADCPs with the CTD package (Fig. 3.6). The following subsection is concerned in how to obtain the final velocity profile from the raw overlapping velocity profiles.

3.2.4 Data Processing

As discussed in the subsection 3.2.1, the velocities estimated by ADCPs are relative velocities. Each ADCP velocity profile can be interpreted as the sum of three parts:

$$U_{\text{ADCP}}(z) = U_{\text{ocean}}(z) + U_{\text{CTD}}(z) + U_{\text{noise}}(z) \quad (3.8)$$

where U_{ocean} represents the unknown velocity profile of the ocean. Typically, U_{ocean} at the same depth is assumed to be constant over the duration of the cast (T) and any space-time variations will be interpreted as U_{noise} . Here U_{CTD} is the horizontal motion of the ADCP that is mounted on the CTD frame. U_{CTD} is assumed to vary slowly in relation to the time between pings. In particular, it can be assumed that U_{CTD} is a constant for each single-ping ADCP profile due to the short time period for each ping. Both U_{CTD} and U_{noise} are unknown. Hence, the existing measurements (U_{ADCP}) and Eq. (3.8) are not sufficient to calculate the current profiles of the ocean (U_{ocean}). Further data processing is required to obtain the solutions. There are two methods that are commonly used to process LADCP data: an implementation of the shear method by Fischer (1990) and a more recent inverse method developed by Visbeck (2002).

Note, that either in the shear method or in the inverse method, the depth of the ADCP is computed at first. The depth can either be found by integrating the vertical velocity of ADCP, $w(t)$ (i.e. the vertical velocity of CTD frame):

$$z(t) = - \int_0^t w(t) dt \quad (3.9)$$

or from a time series of CTD pressure.

Shear Method

According to shear method, U_{ocean} can be interpreted as

$$U_{\text{ocean}}(z) = U_{\text{ocean, barotropic}} + U_{\text{ocean, baroclinic}}(z) \quad (3.10)$$

where $U_{\text{ocean, barotropic}}$ is the barotropic ocean velocity, which is the averaged velocity of currents over the whole depth range of the individual velocity profile; and the baroclinic ocean velocity profile, $U_{\text{ocean, baroclinic}}$ is the part varying with depth.

The ADCP velocity profile (U_{ADCP}) in Eq. (3.8) can also be thought of as the sum of two parts:

$$U_{\text{ADCP}}(z) = U_{\text{ADCP, mean}} + U_{\text{ADCP, variable}}(z) \quad (3.11)$$

As discussed in p.29, the U_{CTD} is constant for each individual ADCP profile. Therefore, only $U_{\text{ADCP, mean}}$ is a function of CTD motion and ocean velocity, while $U_{\text{ADCP, variable}}$ is independent on the CTD motion.

The individual shear profiles are computed from each individual ADCP velocity profile as:

$$S_{\text{ADCP}} = \frac{\Delta U_{\text{ADCP}}}{\Delta z} = \frac{\Delta U_{\text{ADCP, variable}}}{\Delta z} \quad (3.12)$$

The algorithm in Eq. (3.12) that the differences between adjacent elements of the velocity profile ($\Delta U_{\text{ADCP}} = U_{\text{ADCP},j+1} - U_{\text{ADCP},j}$) is scaled by the central depth difference ($\Delta z = z_{j+1} - z_j$), is first differencing. Here Δz (in the following denoted as Δz_{fd}) is called as the vertical first-differencing interval.

The overlapping raw shear profiles are then linearly interpolated and averaged onto a uniform depth grid of interval Δz_g spanning the full water column, yielding an average top to bottom shear profile.

As shown in Eq. (3.10), only the baroclinic ocean velocities are varying with the depth. Hence, vertical integration of the shear profile results in a baroclinic ocean velocity profile $U_{\text{ocean, baroclinic}}$.

Combining Eq. (3.8) and 3.10, $U_{\text{ocean, baroclinic}}$ can be calculated by the following equation

$$\begin{aligned} \int_0^T U_{\text{ocean, barotropic}} dt &= \int_0^T U_{\text{ADCP}} dt - \int_0^T U_{\text{ocean, baroclinic}} dt \\ &\quad - \int_0^T U_{\text{CTD}} dt - \int_0^T U_{\text{noise}} dt \end{aligned} \quad (3.13)$$

In the Eq. (3.13), all the terms are integrated over the cast of duration T , because the time integral of U_{CTD} can be computed as

$$\int_0^T U_{\text{CTD}} dt = \bar{U}_{\text{ship}} T = X_{\text{ship}}^T - X_{\text{ship}}^0 = DX_{\text{ship}} \quad (3.14)$$

where DX_{ship} is the horizontal ship displacement during the cast, that can be inferred from the ship navigation system (e.g. accuracy GPS). Moreover, under the assumption that U_{noise} has no systematic biases, the time integral of U_{noise} is supposed to be zero. Thus the Eq. (3.13) can be simplified as:

$$U_{\text{ocean, barotropic}} = \frac{1}{T} \left(\int_0^T U_{\text{ADCP}} dt - \int_0^T U_{\text{ocean, baroclinic}} dt - DX_{\text{ship}} \right) \quad (3.15)$$

Finally, the whole current profile is estimated by summing $U_{\text{ocean, baroclinic}}$ and $U_{\text{ocean, barotropic}}$ according to the Equation 3.10.

Inverse Method

The fundamental of inverse method is that by means of a set of liner matrix equation to express the relation of the overlapping individual velocity profiles.

$$\mathbf{d} = \mathbf{G}\mathbf{m} + \mathbf{n} \quad (3.16)$$

where the vector \mathbf{d} represents all ADCP velocities U_{ADCP} at different depth from each individual velocity profile. The unknown ocean velocity profile and the motion of CTD package are combined into a single vector \mathbf{m} , that are related to the observations \mathbf{d} by the model matrix \mathbf{G} . The final term, \mathbf{n} represents and imperfect prediction of the true velocity field by $\mathbf{G}\mathbf{m}$.

The matrix Eq. 3.16 can be solved by least squares methods as:

$$\mathbf{m} = [\mathbf{G}^T\mathbf{G}]^{-1}\mathbf{G}^T\mathbf{d} \quad (3.17)$$

One of the advantages of processing the LADCP raw data using the inverse method is that additional information can easily be added to constrain the solution. The new information can be added to the equation array (Eq. 3.16) as one new row. Therefore, in recent years, the inverse method has been widely used to process the raw LADCP data.

Unlike shear method, only velocity profiles can be obtained with the inverse method. The raw LADCP data are smoothed by the model matrix \mathbf{G} , therefore the concrete processes to smooth the data are unknown.

3.3 CTD

CTD stands for Conductivity-Temperature-Depth. CTD instruments measure three important quantities directly: conductivity, temperature and pressure. By measuring conductivity, the salinity of the water mass can be estimated. Because electric current passes much more easily through water with a higher salt content, the salinity of the water is proportional to the conductivity of the water. CTD instruments measure the temperature of the water with the very accurate sensors. CTD instruments measure pressure and the pressure is recorded in decibars. Oceanographers often use decibars as the unit of depth, because 1 m is about 1decibar. The density of water can be calculated from the measurements of conductivity (salinity), temperature and pressure of the water. As the CTD instrument is lowered through the water, measurements of conductivity, temperature and depth are recorded continuously.

The conductivity, temperature and pressure measurements are recorded in digital form. They can be stored by the actual CTD instrument and transferred to a personal computer after the CTD has been brought out of the water or the transfer of data can happen continuously through a cord connected from the CTD instrument to a personal computer on ship.

4

The Model of Polzin et al.

As mentioned in the Introduction, the spectra of the current profiles can be used to infer dissipation rate and eddy diffusivity. Polzin et al. (2002) collected 18 simultaneous XCP-LADCP profile pairs above the Mid-Atlantic in the vicinity of Gibbs Fracture Zone. They computed the vertical shear spectra of the XCP and LADCP profiles. Compared to XCP high resolution measurement from XCP the attenuation of LADCP shear spectrum in the finescale is observed. As mentioned in section 2.2.5, the eddy diffusivities can be estimated from the shear spectra. Hence the accuracy of eddy diffusivity are degraded due to the attenuation in the shear spectrum.

Polzin et al. (2002) therefore analyzed the reasons for the attenuation and built a model spectral transfer function in the finescale. The model spectral transfer function is applied to the LADCP shear spectra. The reproduced shear spectra of LADCP were compared to XCP shear spectra.

Polzin et al. (2002) indicated that the attenuation in the finescale was associated with the sensor geometry of LADCP, sampling strategy, data processing and package motion. They built the transfer function on the basis of quantitatively modeling the attenuation of oceanic shear.

4.1 Transfer Functions for Data Processing

Data processing was considered to be the main reason for the attenuation. Notice that there are two commonly used methods to process LADCP data (see the section 3.2.4). However, the inverse method (Visbeck, 2002) was derived later than the model of Polzin et al. (2002) Therefore, only the shear method was discussed by Polzin et al. (2002). They argued that three processes, range averaging, first-differencing and interpolation, smooth the LADCP data. The smoothing reduce the random errors, but also eliminate some information at the high wave numbers.

Range averaging as mentioned in the section 3.2.3 (p. 26) that is velocities estimated from the received backscattered signals are averaged over the lengths of depth cells. the corresponding spectral transfer function in the ver-

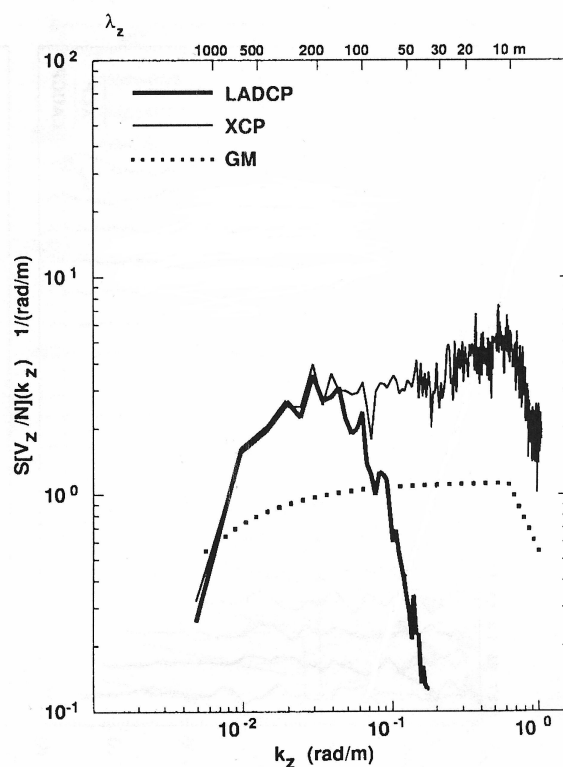


Figure 4.1: Attenuation of LADCP shear spectrum in the finescale, which is compared to XCP shear spectrum. The spectra were estimated from the simultaneous XCP and LADCP profile pairs. The vertical resolution of XCP is higher than that of LADCP (Polzin et al., 2002).

tical wavenumber domain is

$$T_{ra}(k_z) = \text{sinc}^2\left(\frac{k_z \Delta z_t}{2\pi}\right) \text{sinc}^2\left(\frac{k_z \Delta z_r}{2\pi}\right) \quad (4.1)$$

where, $k_z = 2\pi/\lambda_z$ is the vertical wavenumber, function $\text{sinc}(x) = \sin(\pi x)/(\pi x)$, Δz_t is the length of transmitted sound pulse and Δz_r is the length of the depth cell, that are usually set as the same value.

To eliminate unknown package motion U_{CTD} , single-ping velocity profiles are first-differenced, yielding raw single-ping shear estimates (mentioned in the section 3.2.4). This first-differencing is also a main source of smoothing. In the spectral domain, the corresponding transfer function is

$$T_{fd}(k_z) = \text{sinc}^2\left(\frac{k_z \Delta z_{fd}}{2\pi}\right) \quad (4.2)$$

where Δz_{fd} is the vertical first-differencing interval.

The overlapping shear profiles are further smoothed by interpolating and averaging all the single-ping shear profiles onto depth grids of interval Δz_g .

The corresponding spectral transfer function for the interpolation is

$$T_{\text{int}}(k_z) = \text{sinc}^4\left(\frac{k_z \Delta z_r}{2\pi}\right) \text{sinc}^2\left(\frac{k_z \Delta z_g}{2\pi}\right) \quad (4.3)$$

for $k_z < 2\pi/\Delta z_r$.

4.2 Transfer Function for Tilting

Besides data processing, the smoothing is also caused by instrument inclination, or tilt (tilt = $\sqrt{\text{pitch}^2 + \text{roll}^2}$) in vertically varying currents.

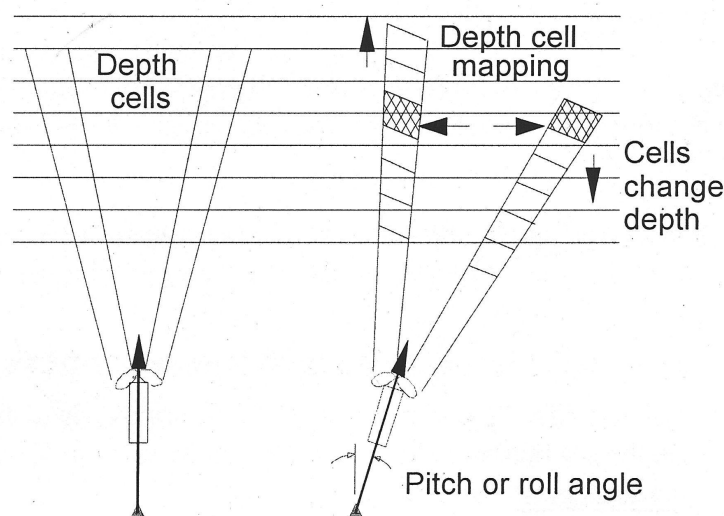


Figure 4.2: ADCP tilt and depth map matching (RDI, 1996).

Fig. 4.2 shows the depth cells of a tilted ADCP. Tilt of the ADCP results in relative depth offsets in depth cells of opposing beams. In Fig. 4.2, for example, the depth cells on the left beam shift slightly upward, and the depth cells on the right beam, that were at the same depth as cells on the left beam, move downward. When the opposing beams are combined to estimate horizontal velocity, the pairs of depth cells are not at the same depth. By means of depth cell mapping, the cells that are around the same depth, for example, the two latticed cells are used to calculate the velocity. However, the depth offset still cause vertical smoothing because these two cells are not exactly at the same depth. The tilt transfer function is involved with the angles of pitch and roll, the horizontally estimated velocity field and the maximum vertical range. Instead of the complicated function, an empirical fit to the resulting transfer function for tilt is

$$T_{\text{tilt}}(k_z) \simeq \text{sinc}^2\left(\frac{k_z d'}{2\pi}\right) \quad (4.4)$$

for vertical wavenumbers $k_z < 0.2 \text{ rad m}^{-1}$ where, for minimum vertical range 16 m (the length of the depth cell employed by Polzin et al.), d' is an empirical constant, $d' = 5.75, 9.0$ and 12.5 m for maximum vertical range $z'_{\max} = 96, 160,$ and 272 m, respectively.

4.3 Transfer Function for Beam Separation Effect

As mentioned in section 3.2.2, the horizontal velocities are estimated from a pair of opposing separated beams under the assumption of horizontally uniform ocean. In fact, the oceanic internal-wave field is not horizontally uniform. Horizontal nonuniformity of the currents degrades the signal in several ways. Firstly, the combination of slant velocities (Eq. (3.6)) smooth both over horizontally varying horizontal velocities and be contaminated by horizontally nonuniform vertical velocities. Secondly, the velocities estimated in the single-ping velocity profiles, that are provided by the lowering of the instrument through the horizontally variable wave field, are averaged over horizontally nonuniform currents. Note that the distance of separation increases with the increasing depth range. Thus, the beam separation effect to each velocity estimates in the each single-ping profile is different. Therefore, the beam separation and instrument lowering transfer function T_{bsl} was the most difficult to evaluate. But the horizontal uniformity of flow is not an unreasonable assumption (discussed in pp. 25). Beam separation effects can be ignored by setting $T_{\text{bsl}} = 1.0$. This setting biases finescale shears slightly low (Polzin et al., 2002).

4.4 Model Summary

The entire transfer function takes into account range averaging, first differencing, interpolation, instrument tilting and beam separation with instrument lowering.

$$\begin{aligned} T_{\text{theo}}(k_z) &= T_{\text{ra}}(k_z)T_{\text{fd}}(k_z)T_{\text{int}}(k_z)T_{\text{tilt}}(k_z)T_{\text{bsl}}(k_z) \\ &= \text{sinc}^2\left(\frac{k_z\Delta z_t}{2\pi}\right) \text{sinc}^8\left(\frac{k_z\Delta z_r}{2\pi}\right) \text{sinc}^2\left(\frac{k_z\Delta z_g}{2\pi}\right) \text{sinc}^2\left(\frac{k_z d'}{2\pi}\right) T_{\text{bsl}}(k_z) \end{aligned} \quad (4.5)$$

The transfer function is applied to the LADCP shear spectra estimated from the LADCP profiles as:

$$S_{\text{transferred}} = T_{\text{theo}}T_{\text{LADCP}} \quad (4.6)$$

to obtain the corrected LADCP shear spectra.

In the study of Polzin et al. (2002), a broadband, 150 kHz ADCP made by RD Instruments was used. Their settings and the settings in this study used for

Terms	Values of Polzin et al.	Values in this study
Δz_t [m]	16	10
Δz_r [m]	16	10
Δz_g [m]	5	10
d'	9	9

Table 4.1: The setting for the model spectral transfer function used by Polzin et al. and used in this study.

the transfer function is listed in the table. the corresponding transfer functions T in dependence on wavenumber, that are computed with the setting listed in Table 4.1, is depicted in Fig. 4.3.

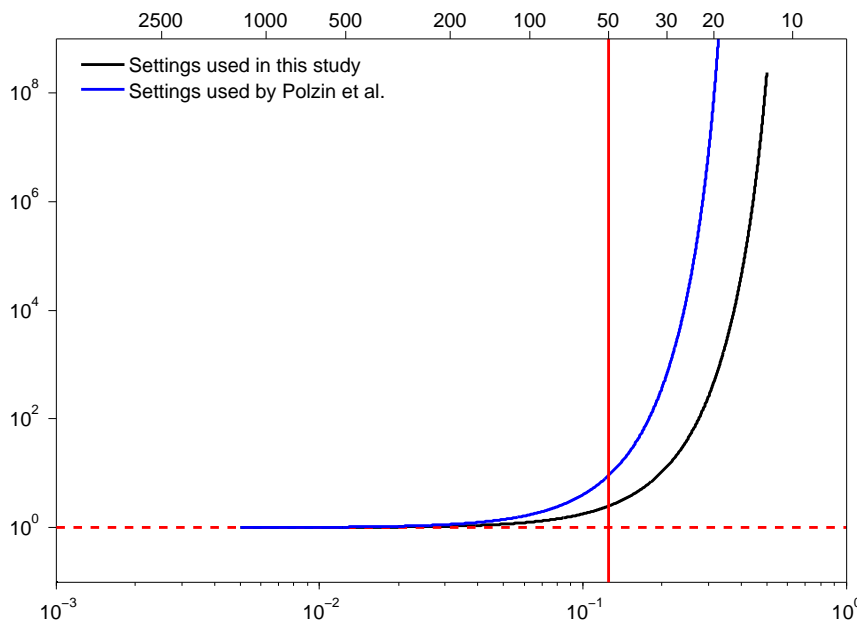


Figure 4.3: Spectral transfer function T_{theo} (Polzin et al. (2002) 2002) in dependence on the wavenumber β that computed with the settings used by Polzin et al. (black) and the setting used in the study (red) listed in Table 4.1.

5

Results

In this chapter, the model spectral transfer function of Polzin et al. (2002) is validated. We validate the model with the same method used by Polzin et al. (2002), but in a different hydrographic region and using a different LADCP instrument.

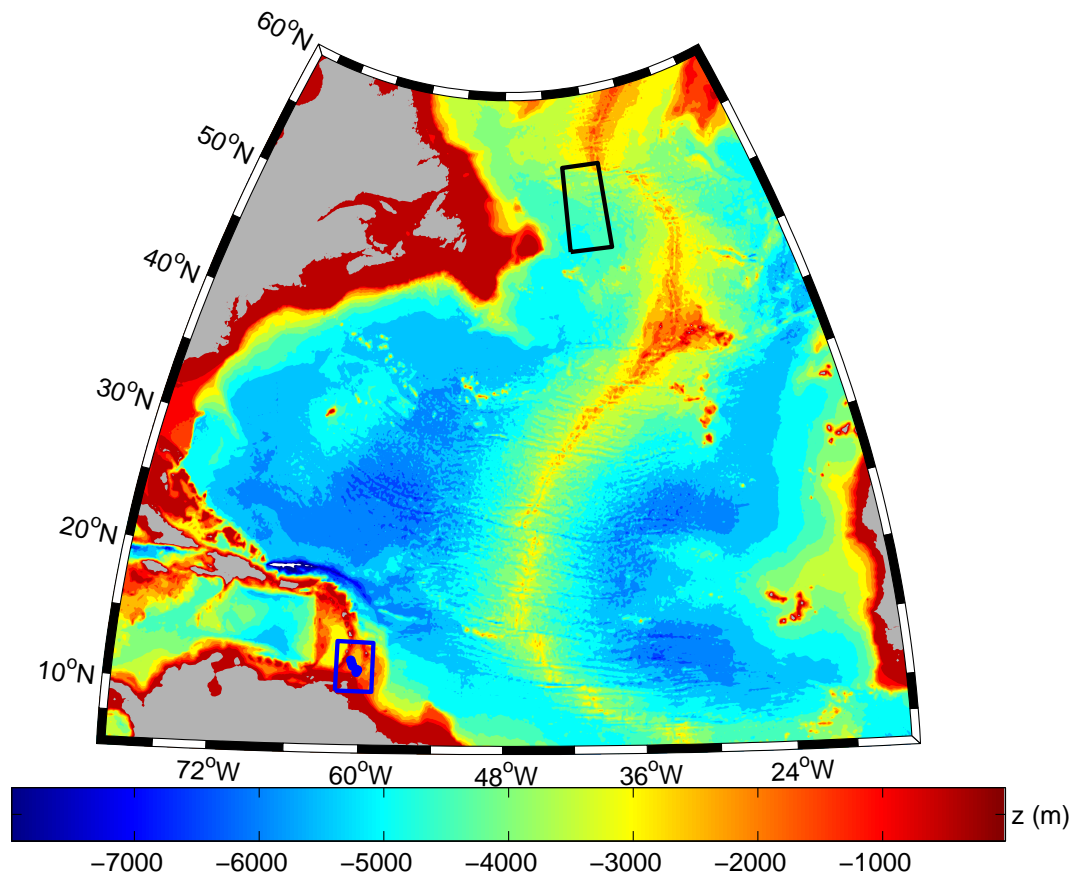


Figure 5.1: Locations of hydrographic stations where the datasets were collected by Polzin et al. (2002) (black frame) and in this study (blue frame). Colors denote bathymetry.

Simultaneous LADCP and XCP casts were carried out during the cruise CARIB-INFLOW with the French research vessel L'ATALANTIC near the lesser An-

Instrument design	instrument used by Polzin et al. (2002)	instrument used during CARIBINFLOW cruise
ADCP frequency	150 kHz	300 kHz
Depth cell length	16 m	10 m
Number of ADCP	one self-contained ADCP	two self-contained ADCPs
Mounting beam angle	30°	20°

Table 5.1: Comparison between LADCP instrument design employed by Polzin et al. (2002) and that used in the caribinflow cruise.

tilles in the western tropical Atlantic. This hydrographic location is far away from the region where Polzin et al. (2002) collected their eighteen LADCP-XCP profile pairs. The data they used were collected above the Mid-Atlantic Ridge in the vicinity of the Gibbs Fracture Zone (Fig. 5.1). Therefore the transfer function built by Polzin et al. (2002) was validated in a different hydrographic region.

Besides the different measurement regions, the LADCP used in this study is more advanced in instrument design than the LADCP employed by Polzin et al. (2002). The comparison of the instruments is shown in table 5.1. The LADCP used during the cruise CARIBINFLOW has the higher frequency. Therefore the vertical resolution is higher than that of velocity profiles collected by Polzin et al. (2002). Because two self-contained ADCPs were employed during the CARIBINFLOW cruise, more ADCP measurements are used for the data processing.

To validate the model of Polzin et al. (2002), the XCP-LADCP profiles were collected and processed. The shear spectra of the XCP and LADCP are estimated by means of Fourier transform. Then the model spectral transfer function is applied to the LADCP shear spectra. The transferred LADCP shear are compared with XCP shear spectra to check if the transferred LADCP shear spectra resemble to XCP shear spectra. The model is further validated by means of comparison of eddy diffusivities that are computed from XCP and LADCP shear spectra respectively.

5.1 Data

During cruise CARIBINFLOW, two self-contained 300 kHz ADCPs with 20° beam angle manufactured by RD Instrument and XCPs manufactured by Sippican were used. The ADCPs were attached to the CTD package. Both velocity profiles and shear profiles were obtained from the LADCP using the shear method (introduced in section 3.2.4). Only the velocity profiles were measured by XCPs. Salinity, temperature and pressure profiles were obtained from a CTD measurement system.

Eight XCP-LADCP profile pairs have been measured during the cruise CARIB-

INFLOW in April 2003 in the hydrographic region $11^{\circ}20' - 12^{\circ}40'N$, $60^{\circ}10' - 61^{\circ}10'W$ (Fig. 5.2). The XCP profile at the station No. 5 is too noisy. It is not used in the further study. Only seven XCP-LADCP profile pairs are used to validate the model spectral transfer function Polzin et al. (2002) in the spectral space. CTD records at the corresponding locations are analyzed for the buoyancy frequency N , and for the spectra of vertical strain λ .

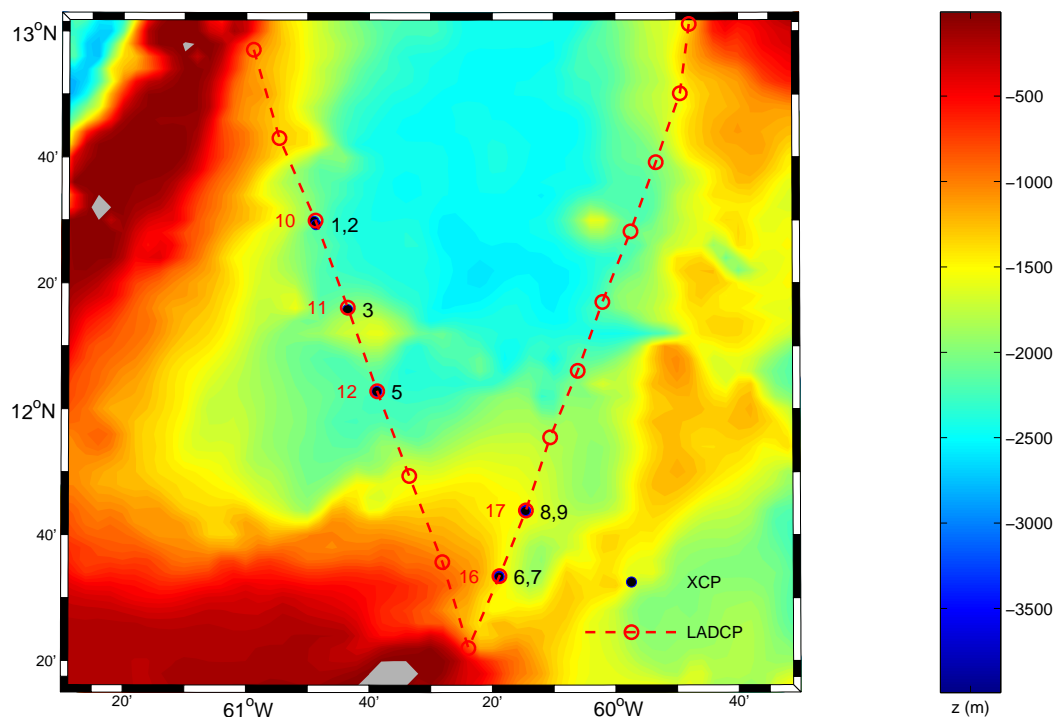


Figure 5.2: Locations of LADCP-XCP pairs near the lesser Antilles in the western tropical Atlantic. Numbers correspond to stations of XCPs (black solid dot) and LADCPs (red hollow circle) profiles which are used in this study. Colors denote bathymetry.

5.2 Comparison of Velocity Profiles

XCP profiles are corrected with LADCP profiles. The first raw XCP-LADCP profile pair is depicted in Fig. 5.3.

The XCP velocity profiles in Fig. 5.3 are very noisy at the beginning of the profile and have obviously extreme values at the end. The noise at the beginning is due to a false time record. The depths of XCP profiles are calculated from the falling time (Eq. (3.3)) which is acquired by PC on the ship. Data acquisition may start on the PC although the XCP probe is still in its launch tube. This makes the vertical offset of the XCP profiles. The noise at the end of the profile may be due to the drag force between the probe and the wire

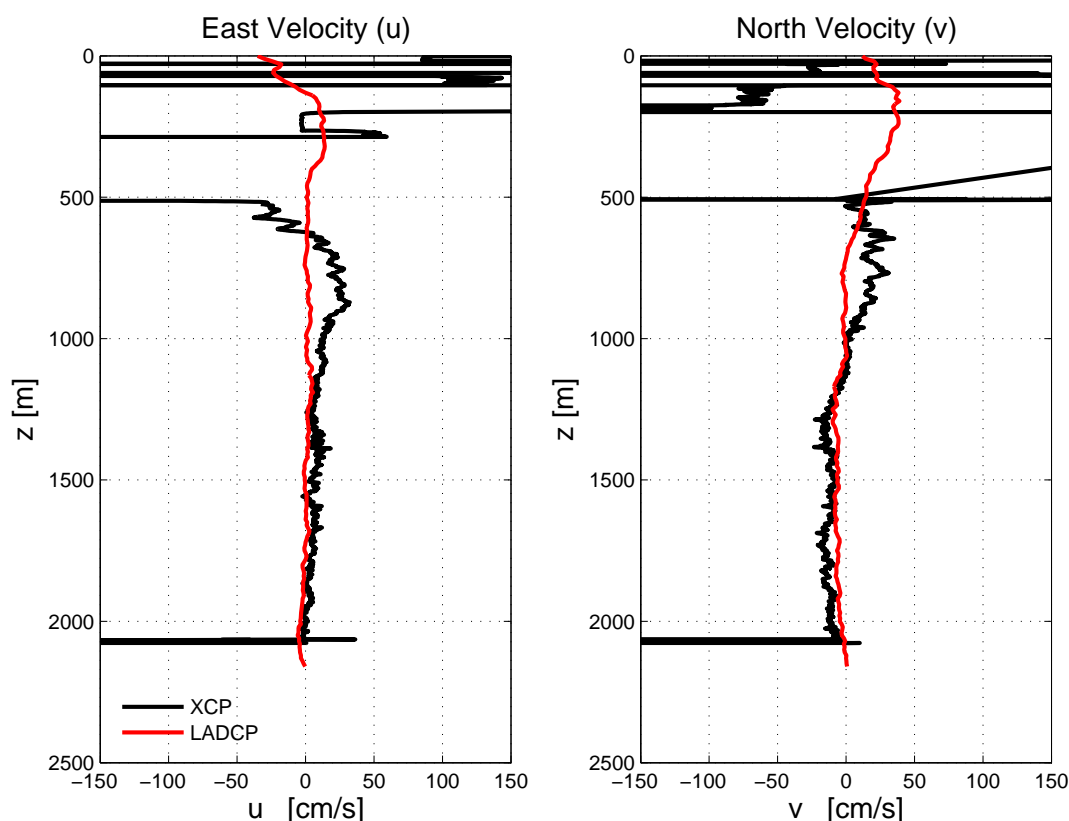


Figure 5.3: Comparison between raw XCP (black) and LADCP (red) u (left) and v (right) velocity profile pair (XCP at station No.1 and LADCP at No.10).

when the measurement is finished. These values are obviously not real current velocities, therefore they should be deleted.

In addition to the vertical offsets, there are horizontal offsets in the XCP profiles, because XCPs only measure the relative velocity (Eq. (3.1) and Eq. (3.2) in section 3.1.1). The offsets are corrected by comparison with the LADCP profiles. The remarkable features of the current profiles are compared to correct the depth and horizontal velocities of XCP profile. The values used to correct the XCP profiles are listed in the table 5.2.

After this correction, XCP and LADCP velocity profile pairs match to each other quite well (Fig. 5.4). Only the XCP profiles at station No. 7 are slightly stretched linearly (depth multiplied by a factor of 1.02). This is reasonable because the XCP velocities are estimated from the fall rate which is not precisely known.

The vertical resolution of raw XCP data are 0.3 m and 0.4 m alternatively. Because the XCP profiles will be Fourier transformed, all XCP profiles are interpolated into uniform depth intervals of 0.5 m.

The corrected XCP profiles are compared with LADCP profiles in Fig 5.4. XCP and LADCP velocity profile pairs resemble each other. The velocity LADCP profiles are smoother than XCP velocity profiles due to their different vertical

Station number	z [m]	u [cm s ⁻¹]	v [cm s ⁻¹]
1	-550	-8	-6
2	-50	-7	6
3	-1400	-17	42
6	-1020	-12	24
7	-22	-7	12
8	-200	5	25
9	0	-6	20

Table 5.2: The vertical and horizontal offsets used to correct the XCP profiles in comparison to LADCP profiles.

resolutions ($\Delta z_{\text{XCP}} = 0.5 \text{ m}$, $\Delta z_{\text{LADCP}} = 10 \text{ m}$). Major differences between the velocity profile pairs are obvious only in the surface layer (about $z < 200 \text{ m}$). These differences are presumably due to the different locations where XCP and LADCP data were collected. In Fig. 5.2 only the positions of the ship are shown. But XCPs were launched about 200 – 300 m away from the ship, because XCPs are sensitive to the magnetic field of the ship and the CTD package. The currents in the surface layer are more variable in temporal and spatial scale than the currents in the deeper ocean, because the currents in the surface layer are driven by wind and other processes. Hence, horizontal velocities in the surface layer are different at the different locations, while the horizontal velocities in the interior ocean are less variable. Thus the XCP-LADCP velocity profile pairs are different in the surface layer but resemble each other in the depth larger than 200 m. The root mean square (rms) velocity differences between the two profiles are not larger than 7 cm s^{-1} for the whole depth range and are typically $2 - 3 \text{ cm s}^{-1}$. In the depth range from 220 m to 1220 m, the rms velocity differences are not larger than 5 cm s^{-1} .

For the seven XCP-LADCP profile pairs shown in Fig. 5.4, the depth range from 220 m to 1220 m is taken to estimate the shear spectra. The upper limit of depth is adopted as 220 m, because of the larger differences between XCP and LADCP profiles in the surface layer. The depth range of XCPs is 1500 m and the depth range of the LADCP is 6000 dbar. Therefore the depth range from 220 m to 1500 m should be used to estimate spectra to give more information of the ocean. Moreover, in the depth range from 220 m to 1500 m, each LADCP profile has 128 data points which is convenient to compute the spectra by means of fast Fourier transform. But due to the operational constraints during the collection of the data, the depth of some LADCP profiles is not larger than 1350 m (for example, the depth range of the LADCP velocity at station No. 6). Therefore, the depth range from 220 m to 1220 m is used to estimate the shear spectra.

Only downcast of LADCP shear profiles are used in this study as Polzin et al. (2002) did, because the measurement time of the XCP profiles corresponds to

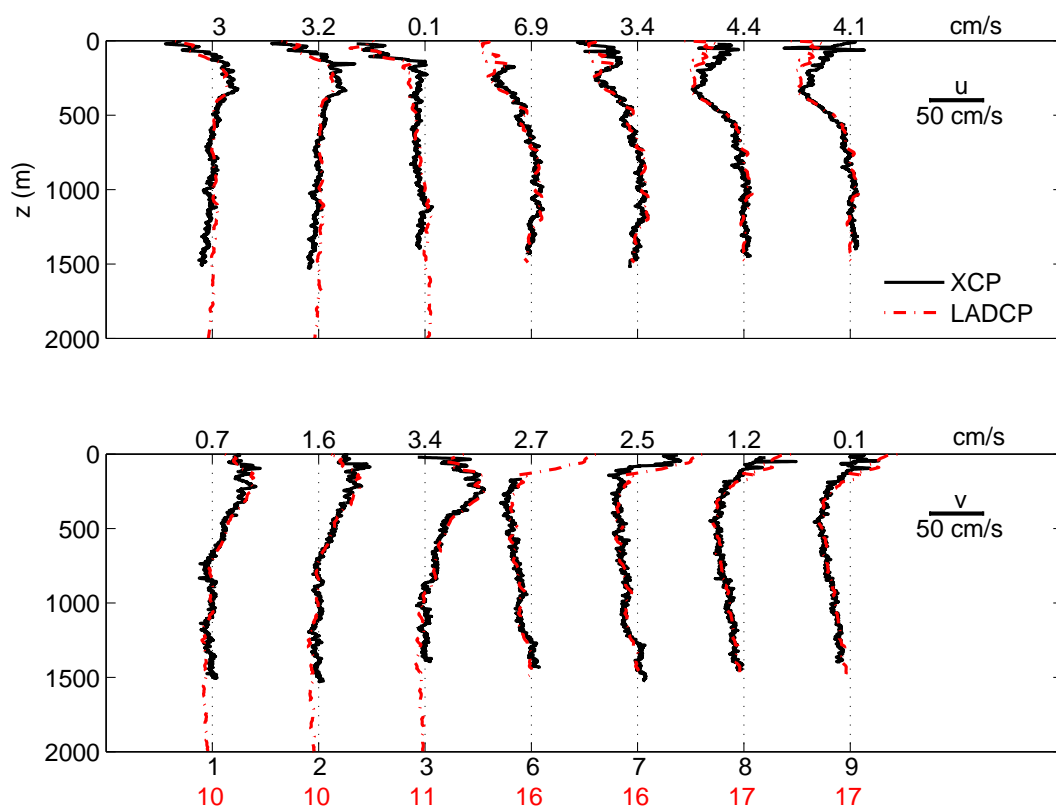


Figure 5.4: Comparison between corrected XCP (black) and LADCP (red) u (top) and v (bottom) velocity profile pairs. Numbers along the upper axis are rms velocity differences between the two profiles. Numbers along the bottom axis are the station numbers of XCP and LADCP respectively. XCP profiles have been linearly stretched and offset to minimize the rms velocity difference between the profile pairs.

the downcast data.

5.3 Spikes in XCP velocity spectra

It is suggested by Sanford et al. (1993) that “spikes” maybe appear in the XCP north velocity spectra (mentioned in section 3.1.3). Spikes are observed in every of our XCP north velocity spectra but not in the XCP east velocity spectra (depicted in Fig. 5.5). Only in the first XCP north velocity spectrum (at XCP station No. 1) the spike is not obvious. The amplitude of the spikes in the other spectra is very high. For the depth range from 220 m to 1220 m, the spikes are found at the wavelength around 25 m in the north velocity spectra. The vertical wavelengths at which the spikes appear vary with the depth of the velocity profiles and for the different XCP probes. It is suggested by Sanford (1982) that the spikes can appear in the north velocity spectrum from the wavelength 10 m to 30 m. The spikes we found are in this wavelength range. Comparing

the north velocity spectra (Fig. 5.5 (left)) with the corresponding rotation frequency (f_{rot}) spectra of the XCPs (Fig. 5.5 (right)), the spikes appear at the same vertical wavelengths. The spikes in the XCP northward velocity spectra are not caused by the high energy at these wavelengths, but created by the XCP instruments. An explanation for the source of the oscillation of north velocity v and the rotation frequency f_{rot} is given in the section 3.1.3.

The XCP spectra are contaminated by the spikes at the wavelength about 25 m. But the XCP and LADCP spectra are compared for the wavelengths larger than 50 m, when the model spectral transfer function of Polzin et al. is validated. The spikes will not influence the validation of LADCP model built by Polzin et al. (2002)

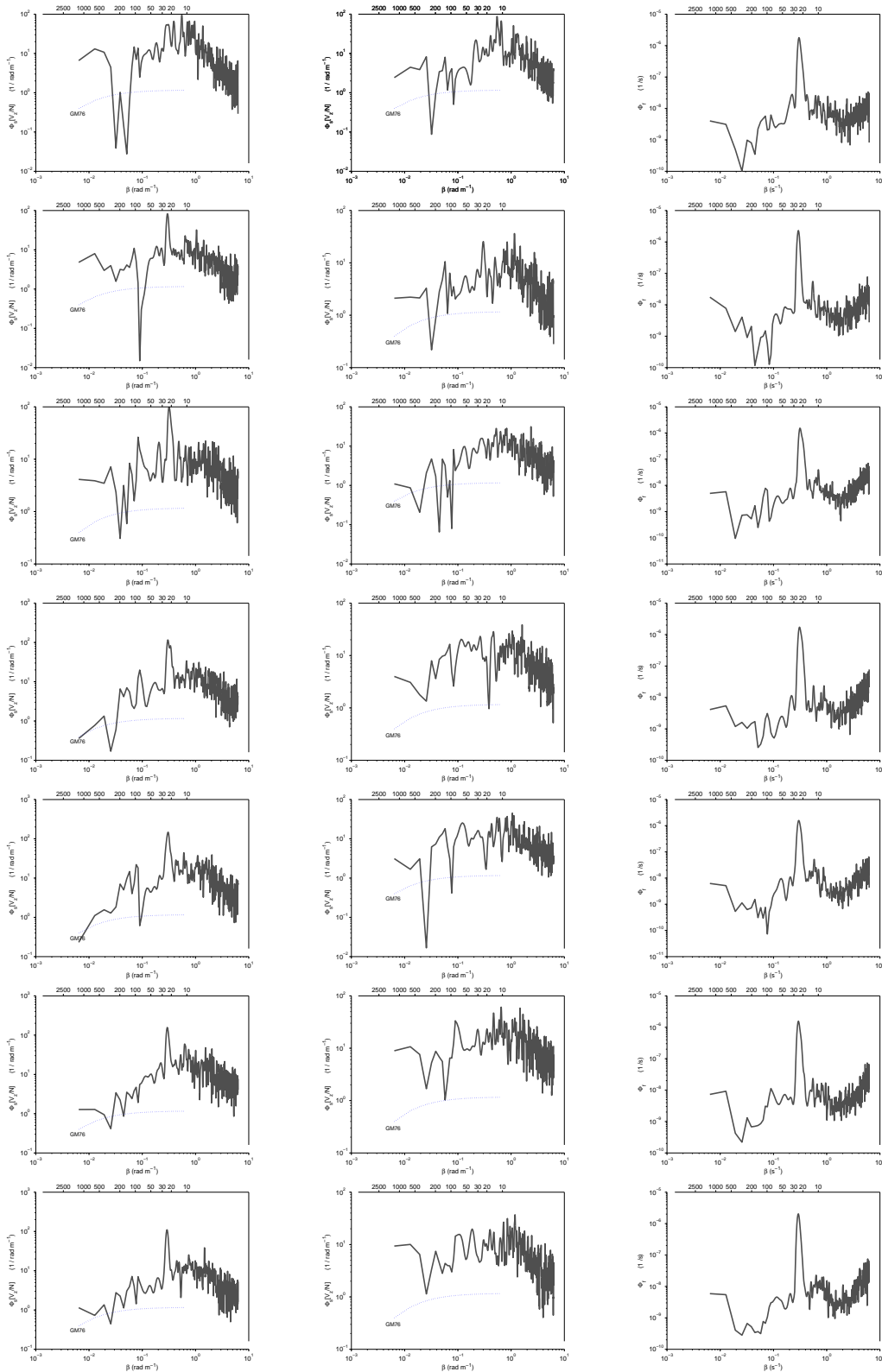


Figure 5.5: North velocity spectra (left), east velocity spectra (middle) and rotation frequency spectra (right) of the XCP profiles in the depth range from 220 m to 1220 m. The spikes appear in every north velocity spectra at the wavelength about 25 m. But the wavelength is varying with different XCP probes. There are no spikes in the east velocity spectrum. The spikes in the rotation frequency spectra are observed at the same vertical wavenumbers as the corresponding north velocity spectra. Columns: the corresponding spectra 1-7.

5.4 Comparison of Shear Spectra

In this section the shear spectra of XCP and LADCP profiles are estimated. The model spectral transfer function of Polzin et al. (Eq. (4.5)) is applied to the LADCP shear spectra in the finescale. The model is validated by means of comparing the transferred LADCP shear spectra with XCP shear spectra. In order to further validate this model, the eddy diffusivities, that are estimated from XCP and LADCP spectra respectively, are compared.

5.4.1 Prior to Estimation of Shear Spectra

In this study, the sampled data are subsets of stochastic processes. The spectra of random processes are themselves random processes. In order to improve spectral estimates, a few steps have to be employed prior to spectral analysis.

The mean and trend are generally removed from the time series as

$$y'_n = y_n - \bar{y}_n - \alpha n \Delta t \quad (5.1)$$

where \bar{y}_n is the mean value for the entire record y_n , and α is the linear trend, n is the number of the time series. It is necessary, because the record mean and trend can distort the low frequency components of the spectrum. But the vertical shears are distributed randomly with depth. This step will not take great effect to the spectra. Here the mean and the trend are removed for the entire depth range in order to analyze the data in a common way.

Then a “window” should be applied to the data, before they are Fourier transformed, as

$$y''_n = y'_n * w_n \quad (5.2)$$

where w_n is the function of the window and y'_n is the detrended data in Eq. (5.1). The classic Hamming window is used in this study. The function for the Hamming window is

$$w_n = 0.54 - 0.46 \cos(2\pi n/N); \quad n = 0, 1, \dots, N - 1 \quad (5.3)$$

where N is the total number of the time series. Through the window, the time series of finite duration is analogous to viewing an infinitely long time series in the shape of the window function. Without window, the sampling process results in spectral energy being “rippled” away from one frequency to a wide number range of adjacent frequencies. The windowed data are brought to zero smoothly at the boundaries so that the periodic extension of the data is continuous in many orders of the derivatives. This minimizes the “leakage” of energy in the spectral domain. After Fourier transform, the data are divided by a scale factor, that is the norm square of the window.

5.4.2 Computation of Buoyancy Frequency

All the shear spectra compared in this study are normalized by the buoyancy frequency N . The normalization is convenient for the computation of eddy diffusivity. Buoyancy frequency is a function of density. The density according to Eq. (2.3), in practice, is not measured, but calculated from pressure, temperature and salinity using the equation of state for sea water. Therefore the values of buoyancy frequency are calculated from CTD data using the sea water package for Matlab.

The average buoyancy frequency \bar{N} calculated over the selected depth range ($220 \leq z \leq 1220$ m) is $3.3 \times 10^{-3} \text{ rad s}^{-1}$ at the location of each XCP-LADCP pair.

5.4.3 Coherence Spectrum of XCP and LADCP profiles

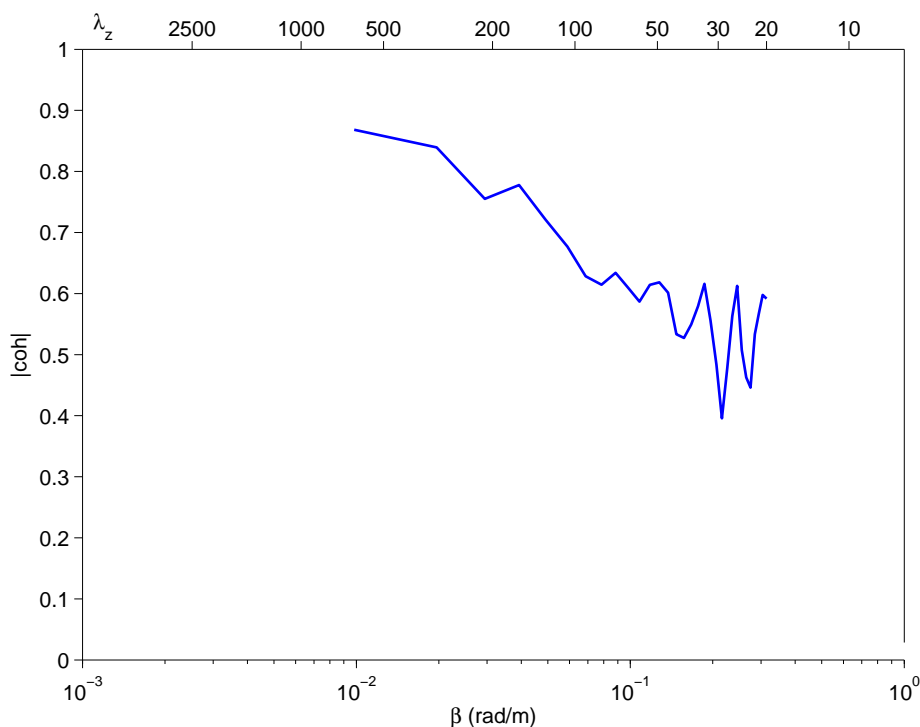


Figure 5.6: Coherence spectrum of XCP-LADCP velocity profiles. The coherence between XCP and LADCP velocity profiles from the depth range 220 m – 1220 m.

Because the model spectral transfer function is validated by means of comparing the transferred LADCP shear spectrum with the XCP shear spectrum, the coherence between XCP-LADCP profile pairs are checked with their coherence spectrum.

The coherence spectrum is computed as

$$\gamma_{\text{XCP LADCP}}^2(\beta) = \frac{|\Phi_{\text{XCP LADCP}}(\beta)|^2}{\Phi_{\text{XCP XCP}}(\beta) \Phi_{\text{LADCP LADCP}}(\beta)} \quad (5.4)$$

where $\Phi_{\text{XCP XCP}}$ and $\Phi_{\text{LADCP LADCP}}$ are one-sided spectra for the XCP and LADCP velocity profiles respectively, and $\Phi_{\text{XCP LADCP}}$ is the one-side cross-spectrum. β is the vertical wavenumber in rad s^{-1} .

The coherency spectrum suggests the correlation of the XCP velocity profiles and LADCP velocity profiles. The coherence of these two spectra should be in the range of

$$0 \leq |\gamma_{\text{XCP LADCP}}^2(\beta)| \leq 1 \quad (5.5)$$

The coherence spectrum is shown in Fig. 5.6. The coherence of them is large ($|coh| > 0.6$ here) for the wavelength larger than about 50 m. The coherence spectrum is contaminated by the noise from the wavelength about 30 m. This shows that XCP and LADCP profiles are correlated quite well. The XCP and LADCP shear spectra should be comparable to each other.

5.4.4 Shear Spectra of XCP and LADCP Profiles

The processed XCP-LADCP profiles are used to compute the shear spectra by means of the Fourier analysis method (see section 2.2.2). As mentioned in section 2.2.4, there are two different methods to estimate the shear spectrum. The shear spectra can be estimated from shear profiles. They can also be converted from velocity spectra.

The XCP shear profiles that are calculated from the velocity profiles according to Eq. (2.17) can not be used to compute the shear spectra directly. Because the vertical resolution of XCP profiles is very high ($\Delta z_{\text{XCP}} = 0.5 \text{ m}$), the XCP shear profiles are very noisy. Compared with the LADCP shear profiles, the root mean square (rms) vertical shear of XCP is about two times larger than that of LADCP, although the mean values of XCP shear and LADCP shear are similar. Vertical shear in the ocean is a small quantity (about 0.1 s^{-1}), therefore the rms vertical shear differences between these profiles are quite large. If the shear spectra of the XCPs are directly estimated from XCP shear profiles, the energy levels of the XCP spectra will be much higher than the energy levels of the LADCP shear spectra. Therefore the shear spectra of the XCP are estimated by means of the velocity spectra. Two horizontal velocity components are combined as $V = u + iv$. Profiles of V are used to estimate the velocity spectrum Φ_u . Then the shear spectra Φ_s are derived from the velocity spectra according to Eq. (2.19).

The shear spectra of the LADCP are estimated directly from shear profiles, because the LADCP shear profiles can be obtained when the raw LADCP data are processed (mentioned in section 3.2.4). The LADCP velocity profiles are computed from the integration of vertical shear. The noise of the vertical shear will

be integrated by this computation. Thus the optimal method to obtain LADCP shear spectra is that the LADCP shear spectra are computed from LADCP shear profiles.

Both XCP and LADCP spectra are smoothed with a 5-point triangular filter for wavelengths smaller than 75 m, in order to obtain a better view of spectra in this wavelength range.

The GM76 model shear spectrum is calculated according to Eq. (2.16) and Eq.(2.21). The GM76 model shows the internal wave spectrum in the open ocean. If spectral density of the shear spectra is higher than that of the GM model spectrum, it means that there are higher energy for vertical mixing.

The vertical shear spectra of the seven XCP-LADCP profile pairs are depicted in Fig. 5.7-Fig. 5.13. The transferred LADCP shear spectra that are reproduced with the model spectral transfer function are plotted into the figures.

The XCP shear spectra and LADCP shear spectra resemble each other. Both XCP shear spectra and LADCP shear spectra are nearly white (spectral density is constant) for wavelength greater than 100 m. The differences of spectra at the low wavenumbers will not have an important effect on the calculation of the eddy diffusivities. This will be shown later in the section 5.4.6. The spectral densities of both XCP shear spectra and LADCP shear spectra are higher than those of GM76 model spectra. That means there is more energy for mixing in the region where the data are collected.

An extremely low spectral density value is observed at the wavelength at about 200 m both in the XCP shear spectrum and in the LADCP shear spectrum (Fig. 5.7). This low spectral density is very strange. But such low power spectral densities (PSD) appear also in the XCP shear spectrum and LADCP shear spectrum in Fig. 5.8, although it is not as low as the PSD value in Fig. 5.7. As in Fig. 5.2 depicted, the corresponding XCP-LADCP profiles were collected at close locations.

In Fig. 5.7 and Fig. 5.8 the energy levels of the XCP shear spectra are higher than the energy levels of the LADCP shear spectra. A possible reason for the differences in energy levels is that the data were collected in different locations as discussed in section 5.2. But for the other XCP-LADCP shear spectrum pairs, the spectral densities are on the same levels.

Because of the high vertical resolution of XCP profiles, the shear spectra of the XCPs give more information in the finescale. Although the noise of the XCP spectra begins at the wavelength about 15 m and the spikes appear in every XCP shear spectra at the wavelength about 25 m, it is obvious that the XCP shear spectra decrease with increasing wavenumbers for wavelengths smaller than 10 m with a slope of -1 . The red spectra (spectral density decreased with increasing wavenumbers) in the wavelength range from 10 m to 1 m is consistent with the composite spectrum of vertical shear of horizontal velocity estimated by Gargett et al. (1981)(Fig. 2.4).

The XCP shear spectra are slightly blue (spectral density increases with

increasing wavenumbers) in the finescale, which denotes the wavelength region from 10 m to 100 m. The blue spectra are obvious in Fig. 5.7, Fig. 5.8, Fig. 5.12, and Fig. 5.13. The blue spectra may be caused by strong mixing in the ocean.

In every LADCP shear spectra the attenuations are observed in the finescale. The spectral densities of LADCP shear spectra in Fig. 5.7, Fig. 5.8, Fig. 5.12, and Fig. 5.13 increase at the end of the spectra. The increase may be due to the instrument noise.

After application of the model spectral transfer function of Polzin et al. the spectral density of the LADCP shear spectra are enhanced in the finescale. The spectral density of the transferred LADCP shear spectra increases with increasing wavenumbers and is larger than the density of the XCP shear spectra for wavelengths smaller than 50 m. The unreasonable increase is due to the instrument noise as discussed by Polzin et al. (2002).

Using all XCP-LADCP shear spectrum pairs, the averaged spectra are calculated in the way that the base 10 logarithm of each shear spectrum is calculated as $(\log_{10} \Phi_s(i))$ at first, then mean $(\overline{\log_{10} \Phi_s})$ of them is computed, finally this mean value is converted back as $10^{\overline{\log_{10} \Phi_s}}$. The method to compute the averaged spectra is necessary, because the differences of power spectral density (PSD) among the shear spectra of the seven XCP-LADCP pairs are large. The lower power spectral densities would be ignored, if we calculate the mean of them directly.

The averaged XCP and LADCP spectra are depicted in Fig. 5.14. The averaged XCP and LADCP shear spectra resemble each other. Both XCP and LADCP spectra are white for the wavelength larger than 100 m. The averaged spectrum of XCP is contaminated by instrument noise for the wavelengths smaller than 15 m. The slope of the XCP spectrum changes at the wavelength of 10 m. The averaged XCP shear spectrum is slightly blue in the finescale. Attenuation of the LADCP spectra is observed beginning at the wavelength of about 100 m. The reproduced LADCP shear spectrum estimated with the spectral transfer function is also depicted in Fig. 5.14. The energy level of the LADCP shear spectrum is enhanced in the finescale, and the transferred spectrum sharply increases with the increasing wavenumbers for wavelengths smaller than 50 m. This increase is due to the noise of the LADCP instrument which is described by Polzin et al. (2002). These details are in accordance with the observation of Polzin et al. (Fig. 4.1).

The spectral density of the averaged XCP shear spectrum is slightly higher than that of averaged LADCP shear spectrum. This is caused by the energy level differences in the first and second XCP-LADCP shear spectrum pairs (Fig. 5.7 and Fig. 5.8). If these two spectrum pairs are removed when the averaged shear spectra are calculated, the averaged XCP shear spectrum and the averaged LADCP shear spectrum are in the same energy level (Fig. 5.15).

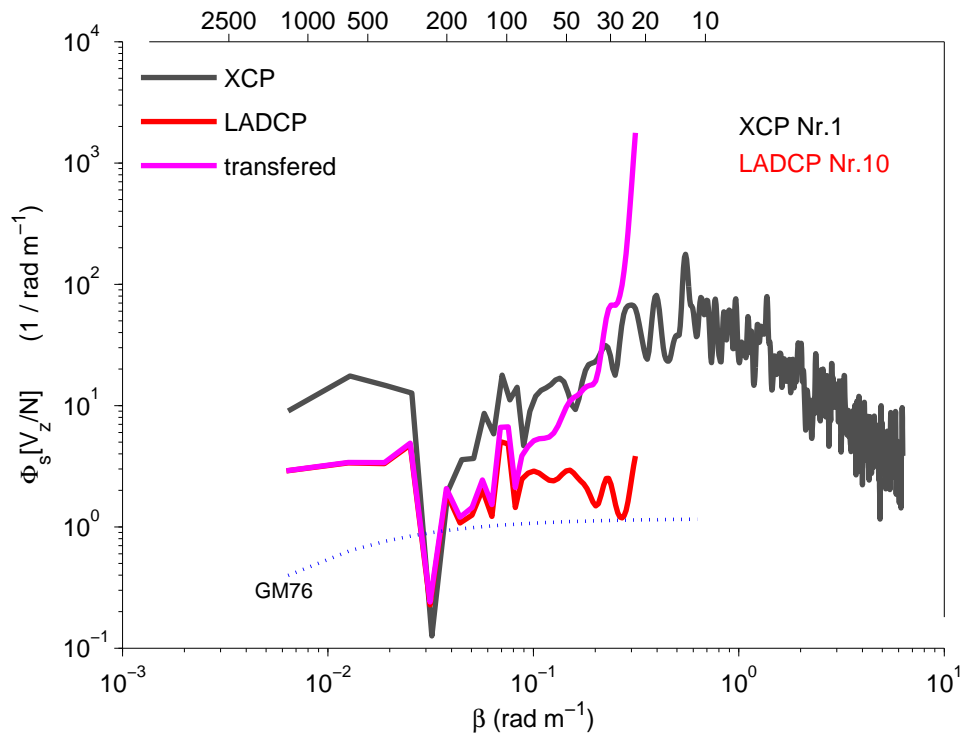


Figure 5.7: Vertical shear spectra of XCP (black) at station No. 1 and LADCP (red) at station No. 10. The corresponding transferred LADCP spectrum is the magenta curve. The GM model spectrum is the blue dotted curve. The same legend is used from Fig. 5.7 to Fig. 5.13. There are differences in the energy level between the XCP shear spectrum and LADCP shear spectrum.

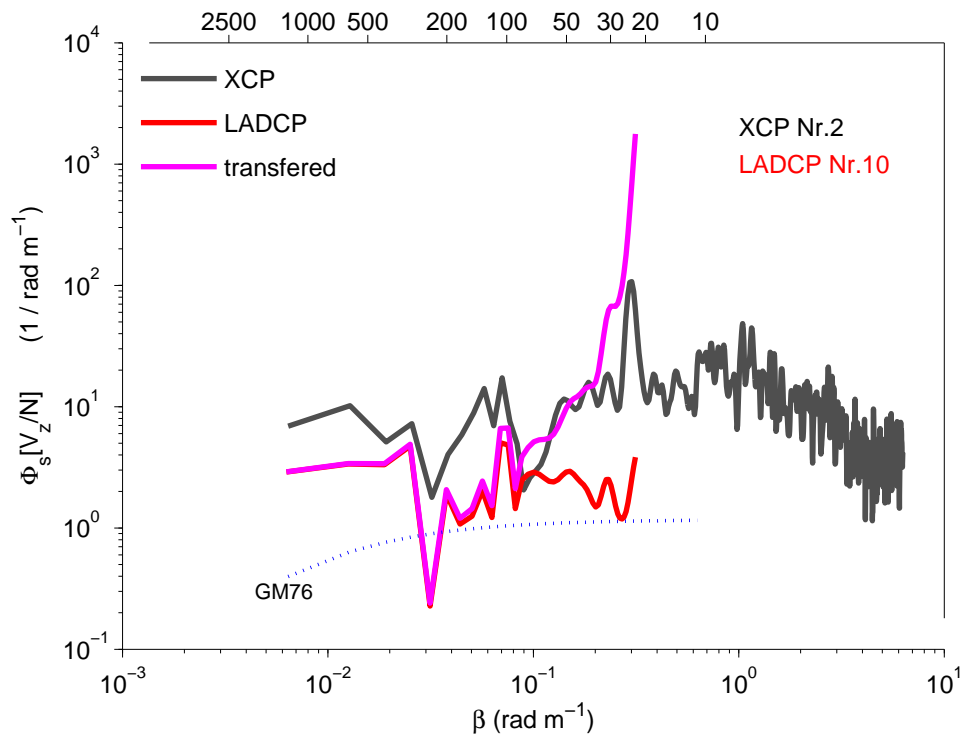


Figure 5.8: Vertical shear spectra of XCP (black) at station No. 2 and LADCP (red) at station No. 10. The difference in the energy levels is similar as in Fig 5.7.

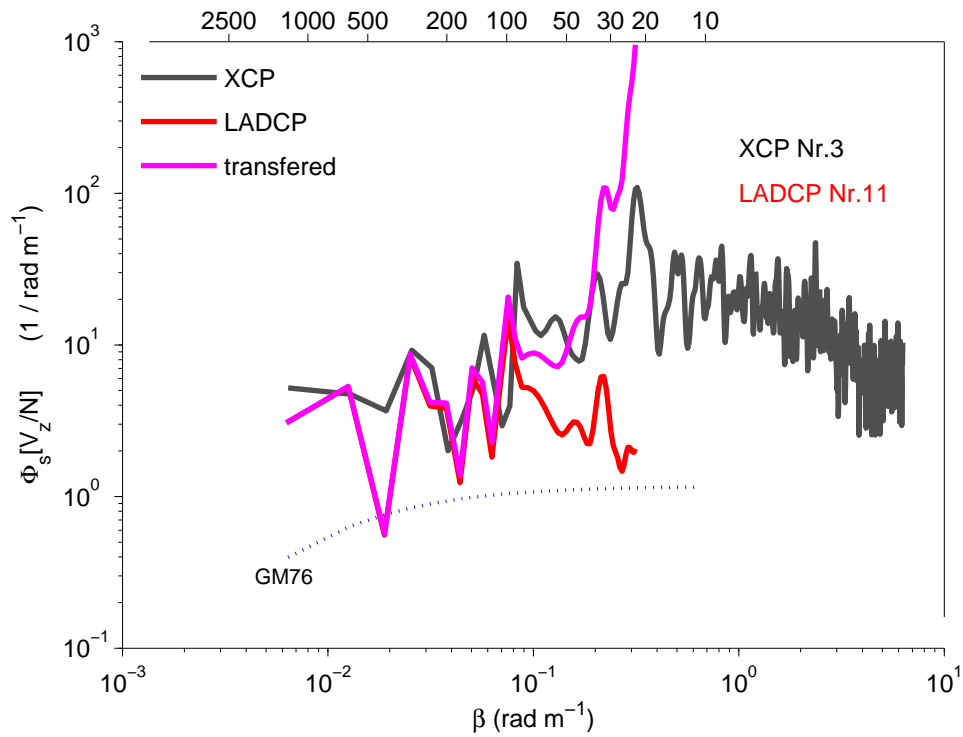


Figure 5.9: Vertical shear spectra of XCP (black) at station No. 3 and LADCP (red) at station No. 11.

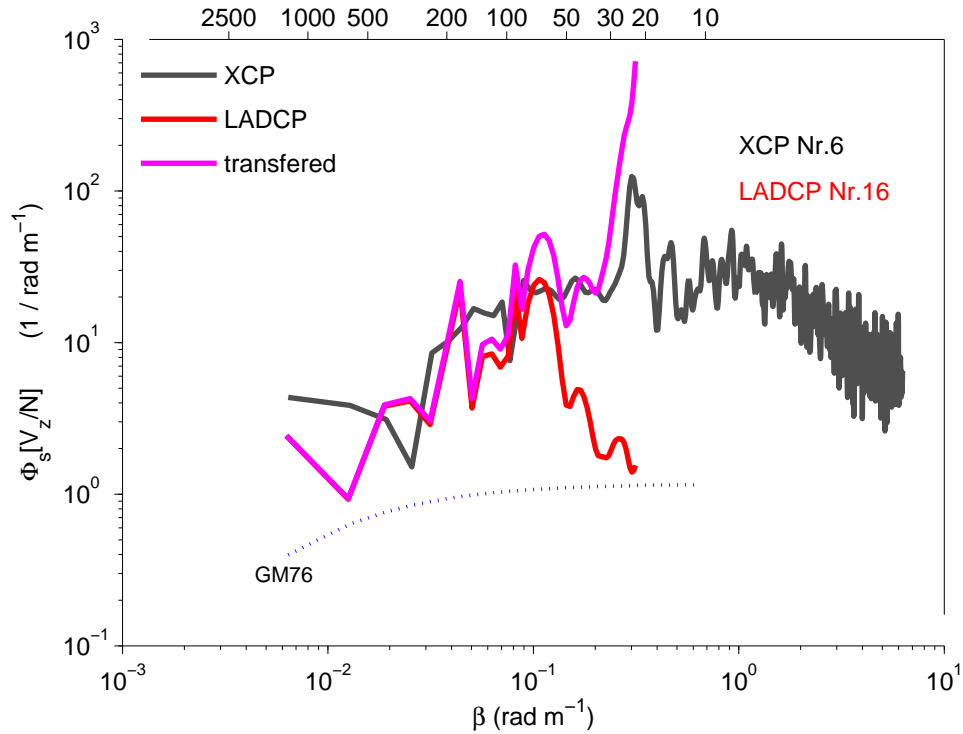


Figure 5.10: Vertical shear spectra of XCP (black) at station No. 6 and LADCP (red) at station No. 16.

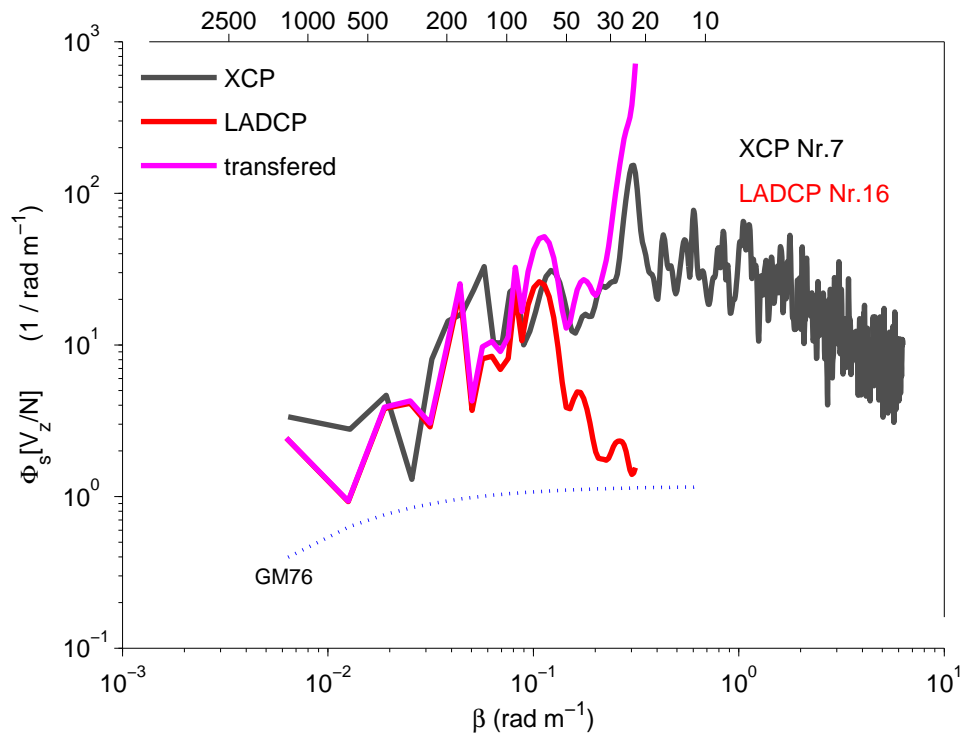


Figure 5.11: Vertical shear spectra of XCP (black) at station No. 7 and LADCP (red) at station No. 16.

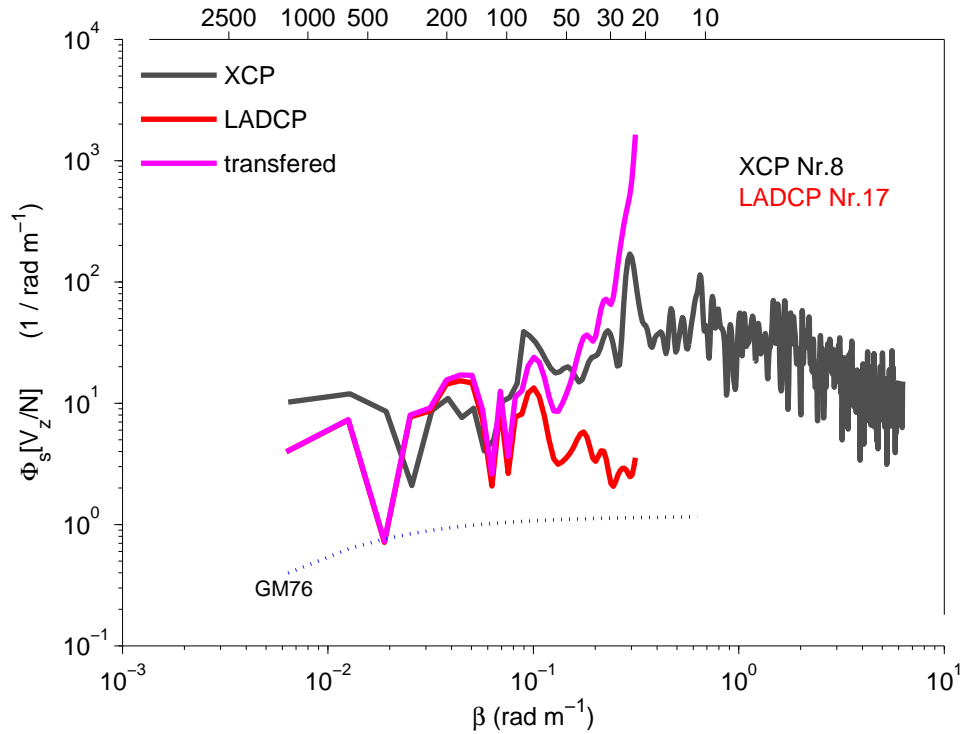


Figure 5.12: Vertical shear spectra of XCP (black) at station No. 8 and LADCP (red) at station No. 17.

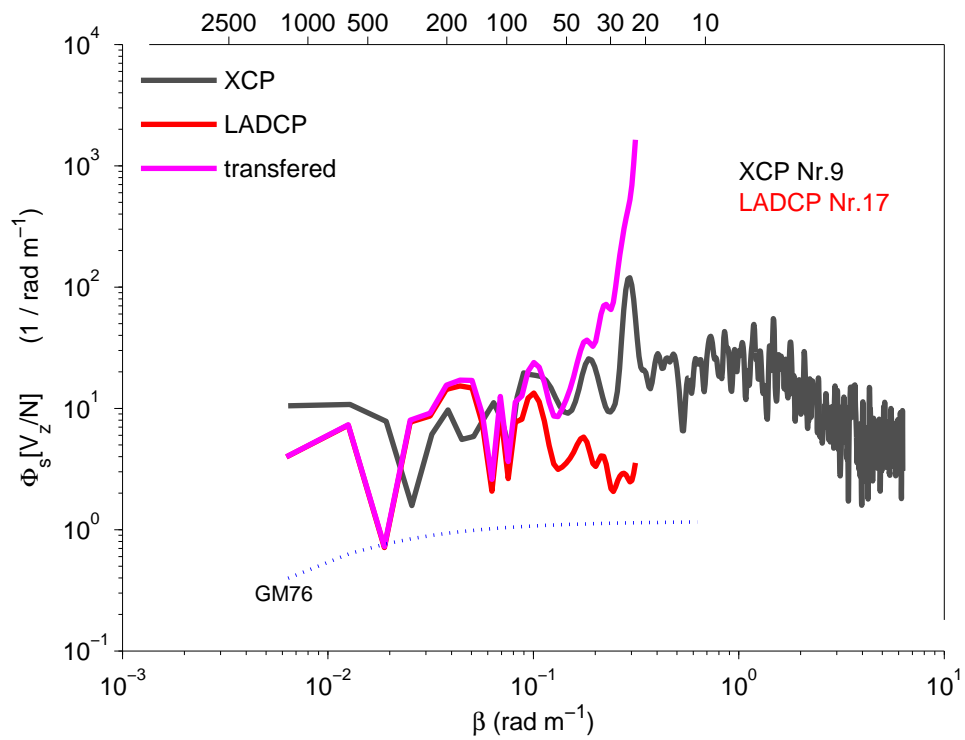


Figure 5.13: Vertical shear spectra of XCP (black) at station No. 9 and LADCP (red) at station No. 17.

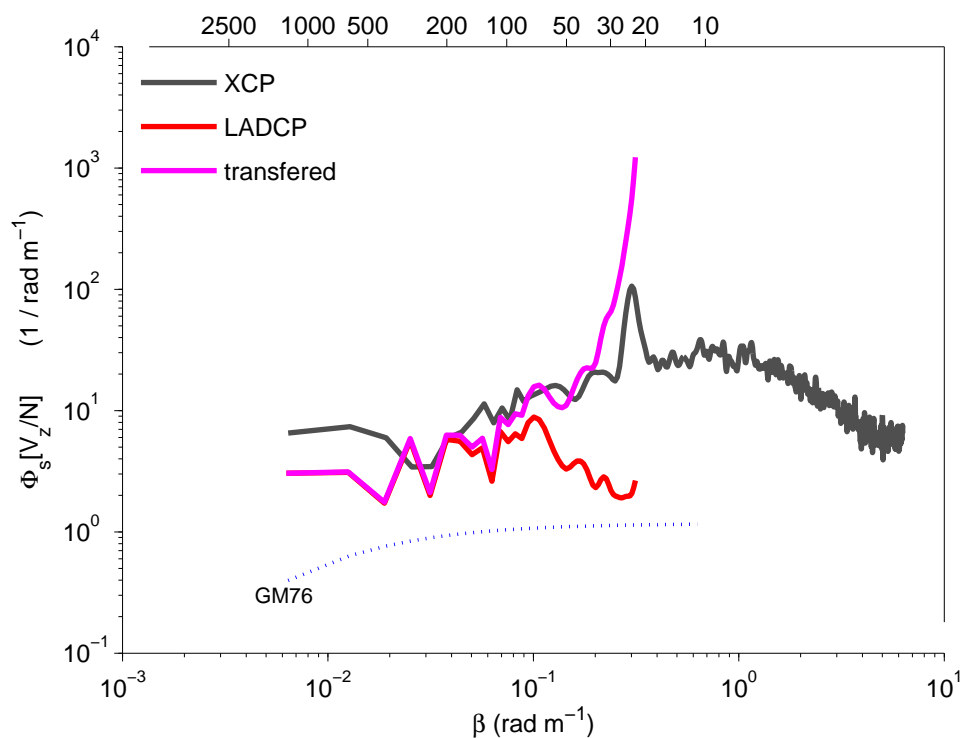


Figure 5.14: Averaged vertical wavenumber shear spectra scaled by buoyancy frequency for the depth range 220 m – 1220 m. XCP shear spectra (black) are converted from velocity spectra. LADCP shear spectra (red) are estimated from LADCP shear profiles. The transferred LADCP shear spectra (magenta) are computed with the spectral transfer function of Polzin et al (Eq. (4.5)). The blue dotted curve is the GM model spectrum

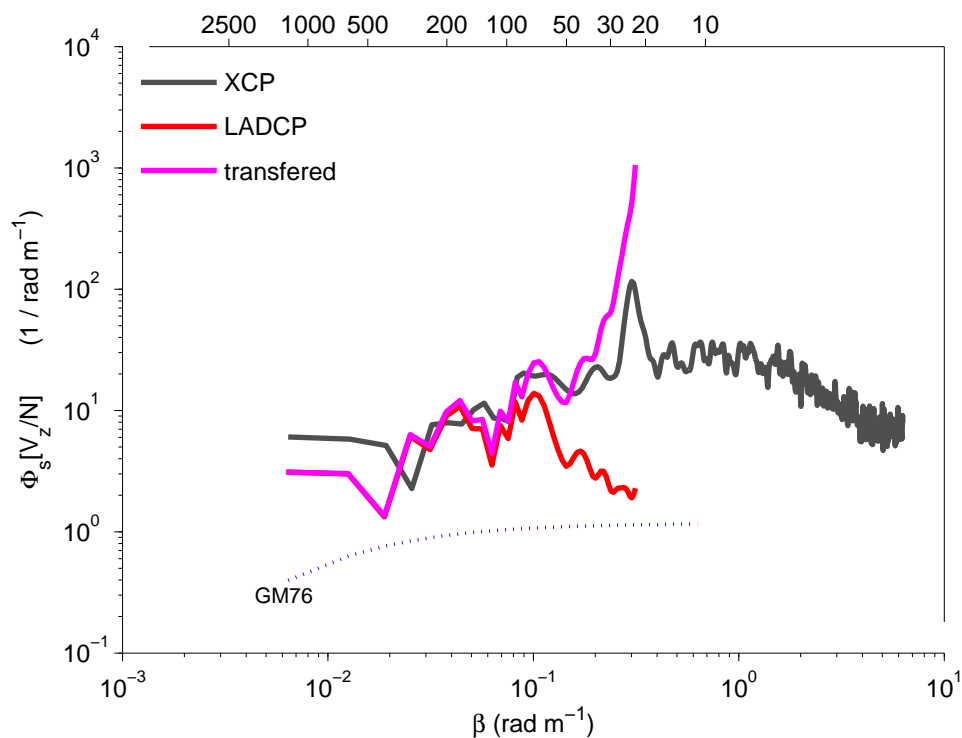


Figure 5.15: Averaged vertical wavenumber shear spectra that are computed with shear spectra in Fig. 5.9-Fig. 5.13. The spectrum pairs in Fig. 5.7 and Fig. 5.8 are removed, when the averaged shear spectra are calculated.

5.4.5 Comparison with Strain Spectra

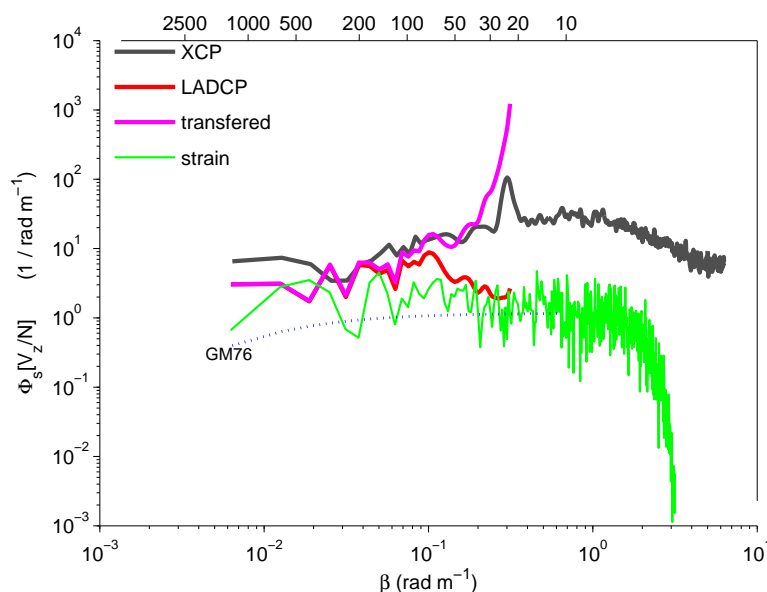


Figure 5.16: Averaged strain spectrum (green). The strain spectra are computed with the method introduced in the section 2.2.4. There is no spike in the averaged strain spectrum. The energy level of strain spectra is lower than the averaged shear spectra of the XCP and LADCP profiles by a factor about 3.

Compared with the GM model spectrum, the higher spectral densities are observed in all the XCP and LADCP shear spectra. In order to verify the strong mixing in the locations where the data were collected, the strain spectra are estimated using the method mentioned in section 2.2.4. The averaged strain spectrum is computed in the same way as the averaged shear spectra are calculated. The averaged strain spectrum is compared with XCP LADCP and transferred LADCP spectra in Fig. 5.16.

The strain spectrum is white for the wavelengths larger than 10 m. The CTD data have a high vertical resolution of 1 m. Note that when the strain profiles are estimated from buoyancy frequency profiles, buoyancy frequency profiles are smoothed a few times. The noise of the strain spectrum begins at the wavelength of about 20 m.

There is no spike in the strain spectrum. It further confirms that the spikes in the XCP shear spectra are created by the instrument, and not by high energy mixing in the wavelength about 25 m.

The energy level of the averaged strain spectrum is lower than the averaged shear spectra of the XCP and LADCP. If the strain spectrum is interpolated onto the same vertical wavenumbers as the XCP shear spectrum or LADCP shear spectrum, the ratio between shear spectrum and strain spectrum is about 3. Because the shear spectra of the XCP and LADCP profiles are normalized by the

buoyancy frequency N , while the strain spectrum is not, the shear to strain ratio is about $3N^2$. The ratio is consistent with the shear to strain ratio of the GM model. The shear spectra and strain spectrum are estimated from the different data. The shear spectra are computed from the XCP and LADCP profiles, while the strain spectrum is calculated from buoyancy frequency profiles. Since both shear spectra and strain spectrum have higher spectral density than the GM model, the strong mixing in the region where data are collected can be confirmed.

5.4.6 Comparison with Eddy Diffusivities

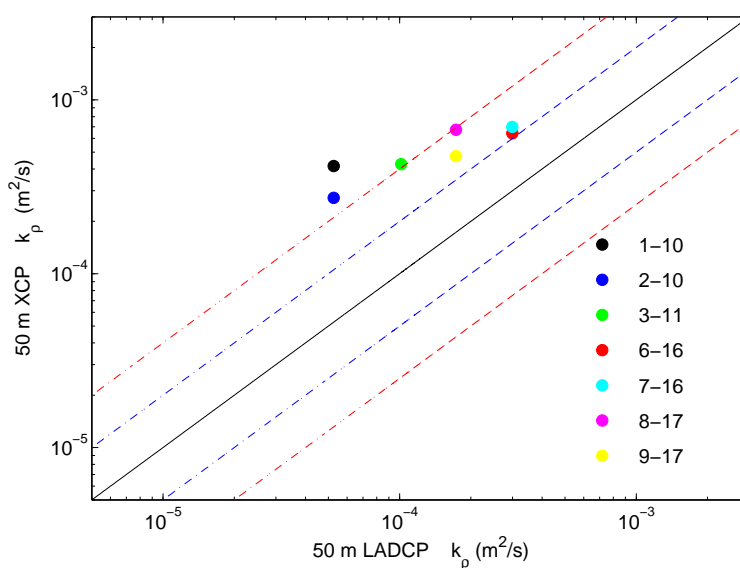


Figure 5.17: Scatterplots of eddy diffusivities for each profile. The XCP inferred eddy diffusivities are larger than LADCP inferred eddy diffusivities, but most of them lie within a factor of 4. The numbers in the legend are the station numbers of XCP (left) and LADCP (right).

To further validate the the model of Polzin et al. the eddy diffusivities estimated from XCP shear profiles and transferred LADCP shear profiles are compared. The eddy diffusivities are calculated using the parametric model mentioned in section 2.2.5. To calculate the shear variances, the shear spectrum is integrated from the minimum of the wavenumber to the wavelength at 50 m (wavenumber $k_z = 0.126 \text{ rad m}^{-1}$), because the transferred LADCP spectra are noisy for the wavelength range smaller than 50 m (the spectra increase sharply in the wavelength range in Fig. 5.14). Moreover, as discussed by Polzin et al. this wavelength range is enough to calculate the eddy diffusivity. The eddy diffusivities of XCP and LADCP are calculated respectively. The eddy diffusivities of XCP and LADCP at the corresponding locations are compared (Fig. 5.17).

Note that although XCP shear spectra vary at the low wavenumbers depicted from Fig. 5.7 to Fig. 5.13, it will not greatly influence the values of eddy diffusivities, because the wavenumbers are very small. Integrated with such small wavenumbers, the differences in spectral density will not result in the large differences in shear variances.

The XCP inferred eddy diffusivities are larger than the LADCP inferred eddy diffusivities. Only the first and the second XCP eddy diffusivities are larger than the LADCP eddy diffusivities by a factor larger than 4. As Fig. 5.7 and Fig. 5.8 depicted, the energy levels of the XCP and LADCP shear spectra are different. This is caused by the different locations where the data were collected. The other eddy diffusivities inferred from XCP and LADCP profiles are very comparable. The XCP eddy diffusivities are also larger than the LADCP eddy diffusivities, but lie within a factor of 4. The factors of 3 – 4 uncertainty for the inferred eddy diffusivity is suggested by Polzin et al. (2002). Besides the first two XCP and LADCP eddy diffusivities, the eddy diffusivities estimated in this study lie in the uncertainty range.

The eddy diffusivities inferred from both XCP profiles and LADCP profiles are larger than the eddy diffusivity measured by the microstructure measurement in the open ocean ($k_\rho = 1.0 - 1.5) \times 10^{-5}$). As Fig. 5.2 depicted, the region where the data were collected is not in the open ocean, the depths at these location are not larger than 2 km. The region is still close to the boundary of the west Atlantic. Strong mixing in this region is reasonable. The current section plots are depicted in Fig. 5.18 showing strong currents. At the LADCP station No. 16, in the depth range from 220 m to 1220 m, the velocity varies with magnitude and the direction (Fig. 5.18). The corresponding largest LADCP eddy diffusivity is found at this station in Fig. 5.17.

The current section plots further confirm the possibility of high energy mixing at the locations where the data were collected. The larger eddy diffusivities inferred from the LADCP profiles are consistent with this strong mixing and lie within the reasonable uncertainty range. The model spectral transfer function can be applied to the LADCP profiles measured by our LADCP and processed with our data processing method.

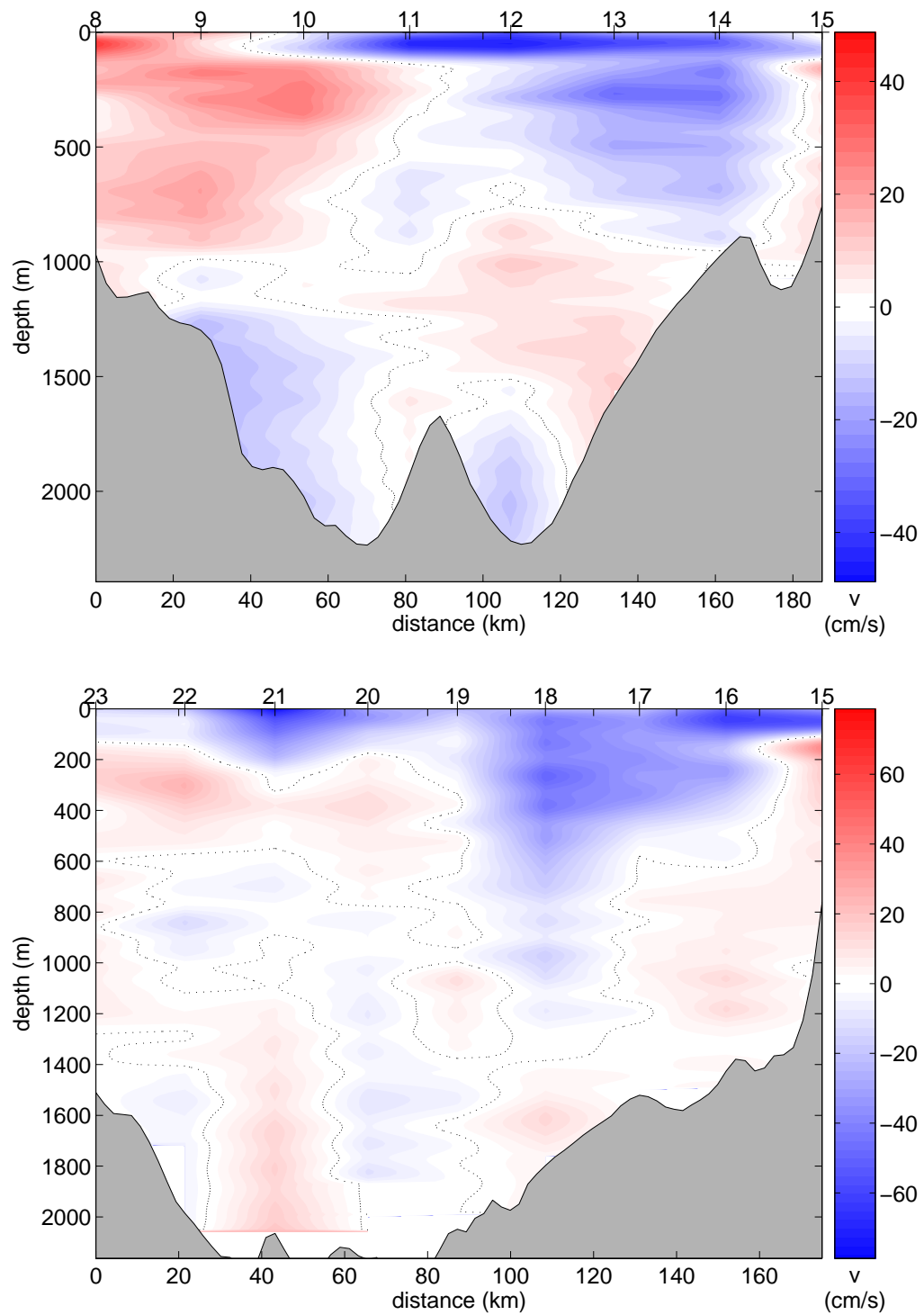


Figure 5.18: Rotated current sections from LADCP measurements. Locations of the two sections are depicted in Fig. 5.2. Velocities are positive in easterly directions, which perpendicular to the sections. Contours denote zero velocity. Top: section with the LADCP stations from No. 8 to No. 15. Bottom: Section with the LADCP stations from No. 23 to No. 15.

6

Summary and Conclusions

The model spectral transfer function of Polzin et al. (2002). is validated using 7 XCP-LADCP pairs obtained during April 2003 in the western tropical Atlantic. Two self contained LADCPs working at 300 kHz have been used in this study. The raw LADCP data are processed with the shear method and the LADCP shear profiles are obtained directly during the data processing. The XCP velocity profiles are corrected by means of comparison with LADCP velocity profiles. After correction, they are quite similar to each other, and the rms velocity differences are typically $2 - 3 \text{ cm s}^{-1}$. The coherency spectrum of the XCP and LADCP velocity profiles is estimated. It shows that XCP profiles and LADCP profiles are correlated to each other with high coherency values for the wavelength larger than 50 m. Hence, the XCP shear spectra and the LADCP shear spectra should be comparable. Note, that the XCP shear spectra are estimated indirectly from the velocity spectra and the LADCP spectra are estimated from the shear profiles. Attenuations are observed in the LADCP shear spectra in the finescale. The model spectral transfer function of Polzin et al. is applied to correct the LADCP shear spectra in the finescale. The reproduced LADCP shear spectra resemble to the XCP shear spectra for the wavelengths larger than 50 m. The XCP and LADCP shear spectra in the wavelength range are used to calculate the eddy diffusivities respectively. The 50m XCP eddy diffusivities are larger than the 50m LADCP eddy diffusivities but most of them lie within a factor of 4 which is in the uncertainty range suggested by Polzin et al. Only the ratio of the 50m XCP eddy diffusivities to 50m LADCP eddy diffusivities at the first and second XCP-LADCP pairs (XCP station No. 1 and LADCP station No. 10; and XCP station No. 2 and LADCP station No. 10) are slightly larger than 4 . The large differences of eddy diffusivities are presumably due to the slightly different measurement locations and times.

Eddy diffusivities are obtained from both XCP and LADCP data. It implies that the turbulence is elevated in the region where the data were collected. The region is located at the western boundary where energetic currents occur. The shear to strain ratio obtained in this study is consistant with the ratio of shear and strain spectra according to the GM76 model.

Although different measurement designs are employed, the model spectral transfer function of Polzin et al. enhances the performance of LADCP shear

spectra in the finescale. It is indicated by the similar shear spectra and the comparable eddy diffusivities of the XCP-LADCP pairs that the model spectral function of Polzin et al. is suitable to our LADCP profiles. It can be used to enhance the performance of the LADCP in the finescale.

Note that the model spectral transfer function of Polzin et al. (2002) was built on the shear processing method. It can maybe not be applied to the LADCP velocity profiles computed with the inverse method. The raw data are smoothed in a different way, when the inverse method is used to process the raw data.

Only 7 XCP-LADCP pairs are used to validate the the model spectral transfer function of Polzin et al. (2002). The statistical reliability should be improved. More simultaneous XCP-LADCP profiles should be employed to validate this model.

The model is only validated in the hydrographic region where the mixing is relatively strong. It can be further validated in the open ocean to check if the model is still sensitive to the weak turbulence.

The different LADCP instrument design can be employed to further validate the model. The settings of the model spectral transfer function are different for different instruments. In this study, only two self-contained 300 kHz ADCPs were used to measure the current profiles.

But because the nice results are obtained in this study, the model of Polzin et al. (2002) can be applied to the shear spectra that are estimated from shear profiles obtained by our LADCP instruments.

Acknowledgments

This thesis was written for the Master degree in the Institute of Environmental Physics in the University of Bremen.

First of all, I want to thank my advisor, Prof. Monika Rhein, for the opportunity to work on such a challenging topic. Thanks to Prof. Justus Northolt for accepting to co-examine this thesis.

Thanks also to my tutor, Dr. Christian Mertens and to Dr. Maren Walter for the guidance and support they have provided throughout the course of this work.

I am also grateful to Prof. Sanford for helping with the problems of xCP data.

I would like to thank Dr. Dagmar Kieke, Dr. Reiner Steinfeldt and Uwe Stöber for helping with the revising draft of this work. Thanks also to Lothar Meyer-Lerbs for his support on the LATEX.

Bibliography

- Bray, N. and Fofonoff, N., 1981: Available potential energy for MODE eddies. *J. Phys. Oceanogr.*, **11**, 1, 30–46.
- Cairns, J. and Williams, G., 1976: Internal wave observations from a midwater float. *J. Geophys. Res.*, **81**, 12, 1943–1950.
- Davis, R., 1994a: Diapycnal mixing in the ocean: Equations for large-scale budgets. *J. Phys. Oceanogr.*, **24**, 4, 777–800.
- Davis, R., 1994b: Diapycnal mixing in the ocean: The Osborn-Cox model. *J. Phys. Oceanogr.*, **24**, 12, 2560–2576.
- Firing, E., 1998: Lowered ADCP development and use in WOCE. *WOCE Newsletter*, **30**, 10–14.
- Fischer, E. and Visbeck, M., 1993: Deep velocity profiling with self-containing ADCPs. *J. Atmos. Ocean. Technol.*, **10**, 764–773.
- Garrett, C. and Munk, W., 1972: Space-time scales of internal waves. *Geophys. Fluid Dyn.*, **2**, 225–264.
- Garrett, C. and Munk, W., 1975: Space-time scales of internal waves: A progress report. *J. Geophys. Res.*, **80**, 3, 291–297.
- Garrett, C. and Munk, W., 2002: Aspects of deep ocean mixing. *J. Phys. Oceanogr.*, **58**, 11–24.
- Gregg, M., 1987: Diapycnal mixing the thermocline: A review. *J. Geophys. Res.*, **92**, C5, 5249–5286.
- Gregg, M., 1989: Scaling turbulent dissipation in the thermocline. *J. Geophys. Res.*, **94**, C7, 9686–9698.
- Gregg, M. and Kunze, E., 1991: Shear and strain in Santa Monica basin. *J. Geophys. Res.*, **96**, C9, 16.709–16.719.
- Henye, F., Weight, J. and Flatte, S., 1986: Energy and action flow through the internal wave field: An eikonal approach. *J. Geophys. Res.*, **91**, 8487–8495.

- Kunze, E., Rosenfeld, L., Carter, G. and Gregg, M., 2002: Internal waves in Monterey submarine canyon. *J. Phys. Oceanogr.*, **32**, 6, 1890–1913.
- Kunzw, E. and Sanford, T., 1996: Abyssdal mixing: Where is not. *J. Phys. Oceanogr.*, **26**, 10, 2286–2296.
- Ledwell, J., Watson, A. and Law, C., 1998: Internal waves in Monterey submarine canyon. *J. Geophys. Res.*, **103**, C10, 21.499–21.529.
- Levine, M., 2002: A Modification of Garrett-Munk interl wave spectrum. *J. Phys. Oceanogr.*, **32**, 11, 3166–3181.
- Mauritzen, C., Polzin, K., McCartney, M., Millard, R. and West-Mack, D., 2002: Evidence in hydrography and density fine structure for enhanced vertical mixing over the Mid-Atlantic Ridge in the western Atlantic. *J. Geophys. Res.*, **107**, A10, 10.1029–10.1114.
- McComas, C. and Müller, P., 1981: The dynamic balance of internal waves. *J. Phys. Oceanogr.*, **11**, 7, 970–986.
- Müller, P., Olbers, D. and Willebrand, J., 1978: The IWEX spectrum. *J. Geophys. Res.*, **83**, C1, 479–500.
- Munk, W., 1966: Abyssdal recipes. *Deep-Sea Res.*, **13**, 707–730.
- Munk, W., 1981: Internal waves and small-scale processes. *Evolution of Physical Oceanography*. Pages 264-291. The MIT Press.
- Osborn, T., 1980: Estimates of the local rate of vertical diffusion from dissipation measurements. *J. Phys. Oceanogr.*, **10**, 1, 83–89.
- Osborn, T. R. and Cox, C. S., 1972: Oceanic finestructure. *J. Fluid Mech.*, **3**, 321–345.
- Polzin, K. and Firing, E., 1997: Estimates of diapycnal mixing using LADCP and CTD data from I8S. *WOCE Newsletter*, **29**, 39–42.
- Polzin, K., Kunze, E., Hummon, J. and Firing, E., 2002: The finescale response of Lowered ADCP velocity profiles. *J. Atmos. Ocean. Technol.*, **19**, 2, 205–224.
- Polzin, K., Toole, J. and Schmitt, R., 1995: Finescale parameterizations of turbulent dissipation. *J. Phys. Oceanogr.*, **25**, 3, 1143–1150.
- RDI, 1996: Acoustic Doppler Current Profiler-principles of operation: A practical primer. *Technical report, RDI*.

- Sanford, T. B., 1982: Velocity profiling: Some exceptions and assurances. *Proc. IEEE Second working Conf. on Current Measurement.*, 101–112. M. Dursi and W. Woodward, eds (IEEE, New York).
- Sanford, T. B., D'Asaro, E. A., Kunze, E. L., Dunlap, J. H. and Drever, R. G., 1993: An XCP User's Guide and Reference Manual. *Applied Physics Laboratory*. 59 pp.
- Sanford, T. B., Dunlap, J. H. and Drever, R. G., 1981: A Comparison of Velocity Profiles Obtained from an Exchangeable Temperature and Velocity profiler (XTVP) and an Acoustically Tracked Profiler at the Atlantic Underwater Test and Evaluation Center (AUTEK). *Applied Physics Laboratory*. 72 pp.
- Toole, J., Ledwell, J., Polzin, K., Schmitt, R., Montgomery, E., St. Laurent, L. and Owens, W., 1997: The Brasil Basin tracer release experiment. *WOCE Newsletter*, **28**, 25–28.
- Toole, J., Polzin, K. and Schmitt, R., 1994: Statistics of the Richardson number: Mixing models and finestructure. *Science*, **264**, 1120–1123.
- Visbeck, M., 2002: Deep velocity profiling using Lowered Acoustic Doppler Current Profilers: Bottom track and inverse solutions. *J. Phys. Oceanogr.*, **19**, 5, 794–807.
- Walter, M., 2003: *Warming of Greenland Sea Deep Water Induced by Abyssal Mixing*. Ph.D. thesis, Universitat Bremen.